

## Causes and Consequences of Diachronous V-Shaped Ridges in the North Atlantic Ocean

Parnell-Turner, Ross; White, Nicky; Henstock, Timothy J.; Jones, Stephen; Maclennan, John C.; Murton, Bramley J.

DOI:  
[10.1002/2017JB014225](https://doi.org/10.1002/2017JB014225)

License:  
None: All rights reserved

*Document Version*  
Publisher's PDF, also known as Version of record

*Citation for published version (Harvard):*  
Parnell-Turner, R, White, N, Henstock, TJ, Jones, S, Maclennan, JC & Murton, BJ 2017, 'Causes and Consequences of Diachronous V-Shaped Ridges in the North Atlantic Ocean', *Journal of Geophysical Research: Solid Earth*, vol. 122, no. 11, pp. 8675–8708 . <https://doi.org/10.1002/2017JB014225>

[Link to publication on Research at Birmingham portal](#)

### **Publisher Rights Statement:**

Article published as: Parnell-Turner, R., White, N., Henstock, T. J., Jones, S. M., Maclennan, J., & Murton, B. J. (2017). Causes and consequences of diachronous V-shaped ridges in the North Atlantic Ocean. *Journal of Geophysical Research: Solid Earth*, 122. <https://doi.org/10.1002/2017JB014225>

### **General rights**

Unless a licence is specified above, all rights (including copyright and moral rights) in this document are retained by the authors and/or the copyright holders. The express permission of the copyright holder must be obtained for any use of this material other than for purposes permitted by law.

- Users may freely distribute the URL that is used to identify this publication.
- Users may download and/or print one copy of the publication from the University of Birmingham research portal for the purpose of private study or non-commercial research.
- User may use extracts from the document in line with the concept of 'fair dealing' under the Copyright, Designs and Patents Act 1988 (?)
- Users may not further distribute the material nor use it for the purposes of commercial gain.

Where a licence is displayed above, please note the terms and conditions of the licence govern your use of this document.

When citing, please reference the published version.

### **Take down policy**

While the University of Birmingham exercises care and attention in making items available there are rare occasions when an item has been uploaded in error or has been deemed to be commercially or otherwise sensitive.

If you believe that this is the case for this document, please contact [UBIRA@lists.bham.ac.uk](mailto:UBIRA@lists.bham.ac.uk) providing details and we will remove access to the work immediately and investigate.

## RESEARCH ARTICLE

10.1002/2017JB014225

## Causes and Consequences of Diachronous V-Shaped Ridges in the North Atlantic Ocean

## Key Points:

- Seismic reflection images of oceanic crust south of Iceland reveal geometry of V-shaped ridges
- Thermal pulsing accounts for V-shaped ridge structure, regional volcanism, and geochemical observations
- Iceland plume is largest on Earth and pulses every 3–8 Ma

## Correspondence to:

R. Parnell-Turner,  
rparnellturner@whoi.edu

## Citation:

Parnell-Turner, R., White, N., Henstock, T. J., Jones, S. M., Maclennan, J., & Murton, B. J. (2017). Causes and consequences of diachronous V-shaped ridges in the North Atlantic Ocean. *Journal of Geophysical Research: Solid Earth*, 122. <https://doi.org/10.1002/2017JB014225>

Received 29 MAR 2017

Accepted 14 AUG 2017

Accepted article online 9 OCT 2017

Ross Parnell-Turner<sup>1</sup> , Nicky White<sup>2</sup> , Timothy J. Henstock<sup>3</sup> , Stephen M. Jones<sup>4</sup>, John Maclennan<sup>2</sup> , and Bramley J. Murton<sup>5</sup>

<sup>1</sup>Department of Geology & Geophysics, Woods Hole Oceanographic Institution, Woods Hole, MA, USA, <sup>2</sup>Bullard Laboratories, Department of Earth Sciences, University of Cambridge, Cambridge, UK, <sup>3</sup>National Oceanography Centre Southampton, University of Southampton, Southampton, UK, <sup>4</sup>School of Geography, Earth and Environmental Sciences, University of Birmingham, Edgbaston, UK, <sup>5</sup>National Oceanography Centre, Southampton, UK

**Abstract** In the North Atlantic Ocean, the geometry of diachronous V-shaped features that straddle the Reykjanes Ridge is often attributed to thermal pulses which advect away from the center of the Iceland plume. Recently, two alternative hypotheses have been proposed: rift propagation and buoyant mantle upwelling. Here we evaluate these different proposals using basin-wide geophysical and geochemical observations. The centerpiece of our analysis is a pair of seismic reflection profiles oriented parallel to flow lines that span the North Atlantic Ocean. V-shaped ridges and troughs are mapped on both Neogene and Paleogene oceanic crust, enabling a detailed chronology of activity to be established for the last 50 million years. Estimates of the cumulative horizontal displacement across normal faults help to discriminate between brittle and magmatic modes of plate separation, suggesting that crustal architecture is sensitive to the changing planform of the plume. Water-loaded residual depth measurements are used to estimate crustal thickness and to infer mantle potential temperature which varies by  $\pm 25^{\circ}\text{C}$  on timescales of 3–8 Ma. This variation is consistent with the range of temperatures inferred from geochemical modeling of dredged basaltic rocks along the ridge axis itself, from changes in Neogene deep-water circulation, and from the regional record of episodic Cenozoic magmatism. We conclude that radial propagation of transient thermal anomalies within an asthenospheric channel that is  $150 \pm 50$  km thick best accounts for the available geophysical and geochemical observations.

**Plain Language Summary** In the North Atlantic Ocean, immense amounts of hot material rises up beneath Iceland from deep within Earth's mantle, forming a gigantic pancake-shaped upwelling. This upwelling, known as the Iceland mantle plume, is the largest on Earth and plays a key role in determining the depth and shape of the North Atlantic Ocean over thousands of kilometers. A pattern of distinctive V-shaped ridges and troughs that are hundreds of kilometers long and tens of kilometers wide occur on the seabed south of Iceland. These V-shaped ridges are thought to have been generated by waxing and waning of the plume, but their precise origin is hotly debated. Here we use an acoustic (i.e., seismic) survey, spanning the North Atlantic Ocean to image these features. We assess competing hypotheses for their formation and argue that they are indeed an indirect record of plume activity through time. Pulses of hot material appear to be generated every 3 to 8 Ma. As they spread beneath adjacent tectonic plates, these pulses cause vertical movements that trigger changes in ancient oceanic circulation.

## 1. Introduction

In the North Atlantic Ocean, the slow spreading Reykjanes and Kolbeinsey Ridges transect the Iceland plume, a major convective upwelling which is thought to transport substantial volumes of mantle material to the Earth's surface (Figures 1 and 2; e.g., Allen et al., 2002; Jones et al., 2014; Morgan, 1971; White, 1997). The most obvious manifestations of this plume are residual depth anomalies of up to 2 km throughout the North Atlantic Ocean, long-wavelength positive free-air gravity anomalies, and low shear wave velocities that extend from the Charlie-Gibbs Fracture Zone to Svalbard, and from Baffin Island to western Norway (Figure 1; Davis et al., 2012; Jones, White, & Maclennan, 2002; Rickers et al., 2013). The plume also has a pronounced geochemical signature that is identified from basaltic rocks dredged from spreading ridges on either side of Iceland (Jones et al., 2014; Murton et al., 2002; Schilling, 1973).

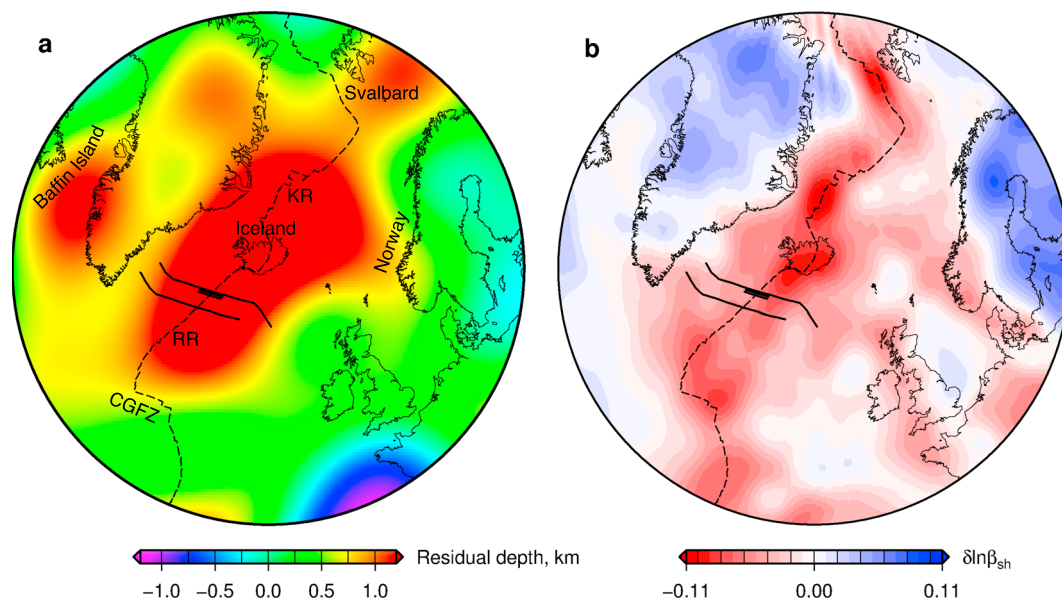


**Figure 1.** (a) Map of residual depth anomalies for North Atlantic Ocean (Gnomonic projection centered on 63.95°N, 17.4°W; Hoggard et al., 2016). Solid black lines = seismic reflection profiles, dashed black line = Mid-Atlantic Ridge, RR = Reykjanes Ridge, KR = Kolbeinsey Ridge, CGFZ = Charlie-Gibbs Fracture Zone. (b) Horizontally polarized shear wave velocity anomalies,  $\beta_{sh}$ , at depth of 120 km taken from full-waveform tomographic model of Rickers et al. (2013).

The short-wavelength structure of oceanic crust on either side of the Reykjanes Ridge is usually interpreted as an indirect record of time-dependent mantle convective circulation. In this interpretation, hot mantle material ascends the plume conduit and spreads out radially beneath the lithospheric plates (e.g., Ito, 2001; Jones, White, & MacLennan, 2002; Navin et al., 1998; Parnell-Turner et al., 2013; Smallwood & White, 1998; White et al., 1995; Vogt, 1971). A striking manifestation of this time-dependent behavior is a set of diachronous V-shaped ridges (VSRs) and troughs which straddle the ridge axis. On Neogene oceanic crust, these features are clearly resolved by the free-air gravity field (Figure 2b). Although linear gravity anomalies also occur on Paleogene oceanic crust, the sedimentary cover is much thicker and interpretation of these weaker anomalies is less certain. North of Iceland, symmetric V-shaped ridges and troughs flank the Kolbeinsey Ridge, although the associated linear gravity anomalies are obscured by sedimentary cover (Hooft et al., 2006; Jones, White, & MacLennan, 2002).

Vogt (1971) suggested that the VSRs are caused by minor crustal thickness changes that are generated when pulses of anomalously hot asthenosphere advect horizontally away from the center of the plume. He proposed two alternative models that could account for the geometry of VSRs. In the channel flow model, asthenospheric pulses are confined to, and flow along the length of, the mid-oceanic ridge and straight VSRs are produced if the velocity of each pulse is constant. Thus, diachronous ridges and troughs are manifestations of changes in oceanic crustal thickness formed at the spreading center when a thermal anomaly is horizontally advected beneath the center. In the radial flow model, asthenospheric pulses flow radially away from the center of the plume. Since velocity decreases as a function of distance, radial flow should produce curved VSRs. However, almost straight VSRs can be generated provided the volume flux of the plume is large which means that the geometry of these VSRs alone cannot be used to discriminate between these alternative models.

Since Vogt's early insight, the origin and significance of these VSRs has been the subject of debate. Part of this debate has focused on whether the melt anomalies required to generate VSRs are caused by thermal or compositional changes within the mantle source region (e.g., Foulger & Anderson, 2005; Martinez & Hey, 2017; Vogt, 1971). A combination of seismic reflection and wide-angle imaging, geochemical analysis of dredged basaltic rocks, and convective modeling have led to the widely held view that the diachronous geometry of VSRs is generated by thermal anomalies that propagate either radially or axially through a  $150 \pm 50$  km thick asthenospheric layer (Figure 3a; e.g., Albers & Christensen, 2001; Ito, 2001; Jones, White, & MacLennan, 2002, 2014; Parnell-Turner et al., 2014; Poore et al., 2011; White et al., 1995; White & Lovell, 1997; Vogt & Avery, 1974). Fluid dynamical calculations suggest that these anomalies could be generated by the periodic generation

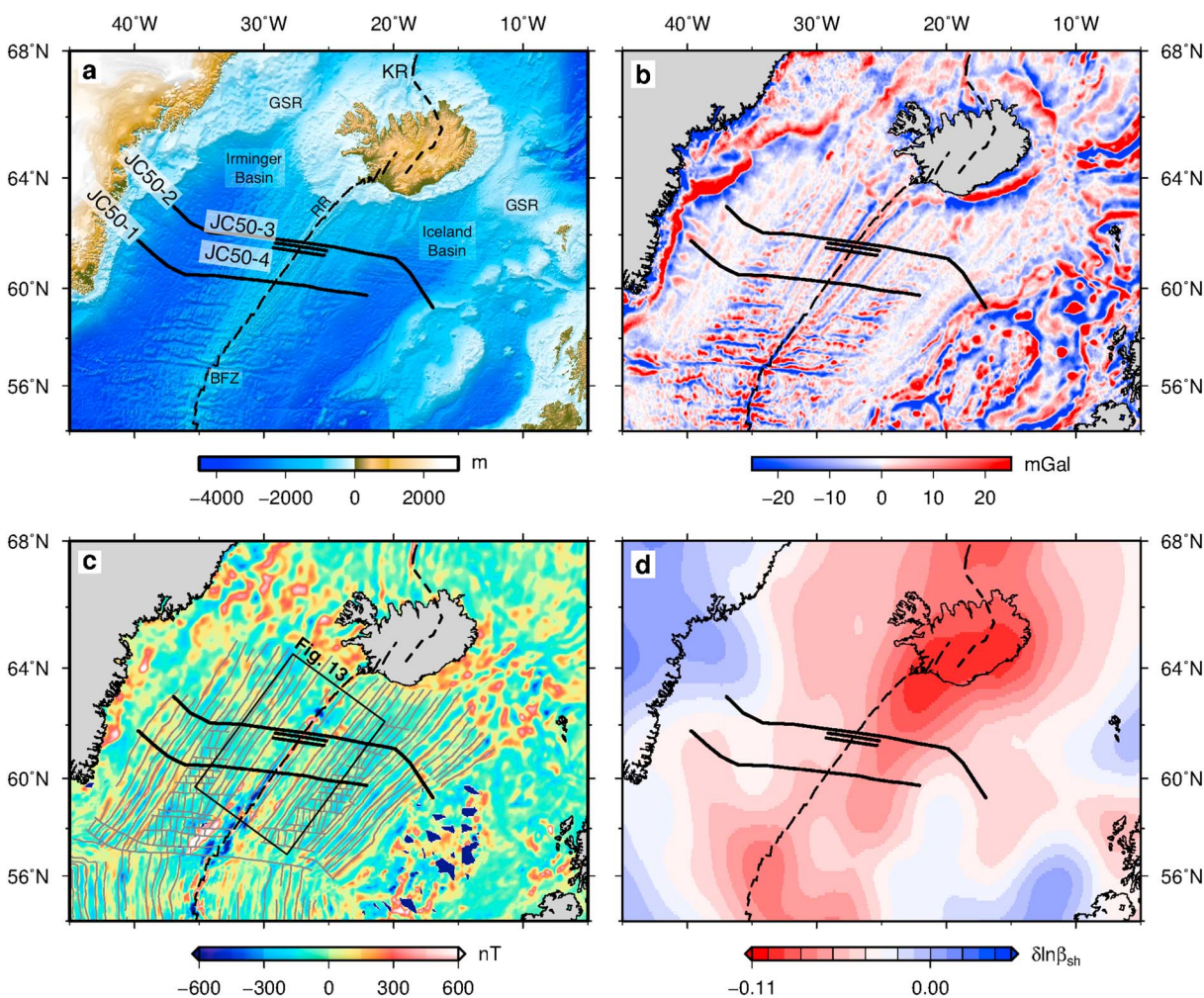


**Figure 2.** (a) Bathymetric map of North Atlantic Ocean showing location of seismic reflection experiment (Mercator projection). Solid black lines = seismic reflection profiles JC50-1, 2, 3, and 4, dashed black line = Mid-Atlantic Ridge, RR = Reykjanes Ridge, KR = Kolbeinsey Ridge, GSR = Greenland-Scotland Ridge, BFZ = Bight Fracture Zone. (b) Satellite free-air gravity anomaly map high-pass filtered to remove wavelengths  $>250$  km (Sandwell et al., 2014). (c) Magnetic anomaly map (Maus et al., 2009). Box = location of Figure 13; gray lines = magnetic isochrons and fracture zones (Jones, White, & MacLennan, 2002). (d) Horizontally polarized S wave velocity anomalies,  $\beta_{sh}$ , at depth of 120 km taken from full-waveform tomographic model of Rickers et al. (2013).

of instabilities within the thermal boundary layer at the base of the plume's conduit (e.g., Ito, 2001; Olson & Christensen, 1986; Schubert et al., 1989).

Recently, two alternative hypotheses for the formation of VSRs have been put forward. The first hypothesis suggests that VSRs are generated by rift propagation, obviating the need for thermally or compositionally generated melt anomalies (Figure 3b; Benediksdóttir et al., 2012; Briais & Rabinowicz, 2002; Hey et al., 2010, 2016). A sequence of propagating rifts and transform faults are envisaged, leading to asymmetric accretion along the ridge axis. In this scheme, V-shaped ridges and troughs are thought to represent pseudofault scarps. A second hypothesis argues that buoyant instabilities upwell along the mid-oceanic ridge axis to generate the observed crustal structure, which avoids the requirement for rapid plume flow altogether (Figure 3c; Martinez & Hey, 2017; Murton et al., 2002).

In order to address these competing hypotheses for VSR formation, we present and analyze regional seismic reflection profiles that were acquired along flow lines between 60 and 62°N south of Iceland. These profiles can be used to analyze the detailed structure of VSRs and to gauge the mode of crustal accretion through time, by determining the amount of spreading that is taken up by brittle extension on normal faults. Residual depth measurements are then used to construct a chronology of Cenozoic V-shaped ridge activity and to estimate asthenospheric potential temperatures through time. These temperatures are compared with those determined from geochemical analysis of basaltic rocks dredged along the Reykjanes Ridge. Alternative

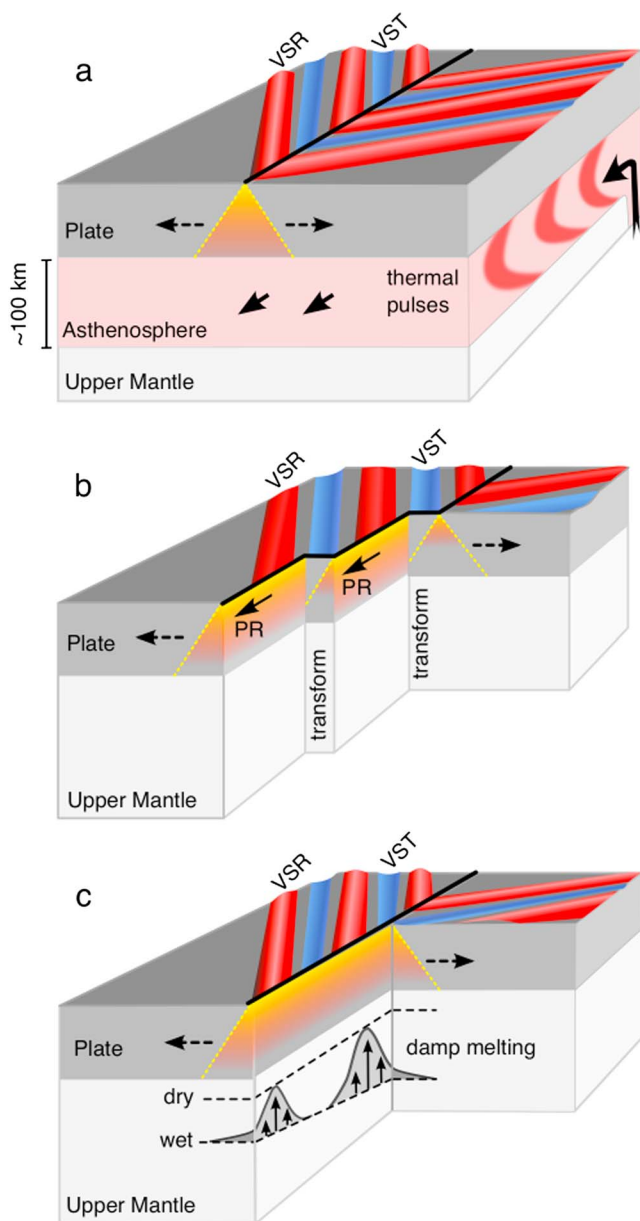


**Figure 3.** Cartoons showing competing hypotheses for VSR formation. (a) Thermal pulsing hypothesis (Vogt, 1971). Dark gray blocks = lithospheric plates, pink block with red patches = asthenospheric channel containing thermal pulses, light gray block = upper mantle, solid arrows = propagation direction of thermal pulses, dashed arrows = plate spreading direction, yellow shaded area = melting region, red/blue ribs = V-shaped ridges/troughs, black line = mid-ocean ridge. (b) Propagating rift hypothesis (Hey et al., 2010). Solid arrows = propagating rift direction. VSRs regarded as failed rifts with thicker crust and V-shaped troughs regarded as pseudofaults that propagate along-axis generating thinner crust. (c) Buoyant mantle upwelling hypothesis (Martinez & Hey, 2017). Gray blobs = buoyant upwelling cells that generate damp melting and thicker crust in absence of thermal anomaly, group of small vertical arrows = vertical upwelling within a given cell, dashed lines = dry/wet solidi.

hypotheses for VSR formation are tested using a combination of these observations together with regional magnetic and gravity data.

## 2. Seismic Reflection Survey

During Cruise JC50 in July–August 2010, >2,400 km of two-dimensional (2-D) multichannel reflection seismic data were acquired (Figure 2). The two longest profiles, JC50-1 and JC50-2, are oriented parallel to plate spreading flow lines and are each >1,000 km long. JC50-1 intersects the Reykjanes Ridge at the southernmost tip of the youngest VSR at 60.2°N. JC50-2 intersects the Reykjanes Ridge 175 km further north at 61.7°N. JC50-1 and JC50-2 span the Icelandic and Irminger basins. Two shorter flow lines, JC50-3 and JC50-4, were also acquired, which are each 218 km long. These profiles cross the mid-oceanic ridge at 61.3°N and 61.5°N, respectively.

The availability of regional flow lines is crucial because it means that reconstructed sediment-basement geometries on either side of the Reykjanes Ridge are exactly conjugate to each other. This feature enables reliable analysis of potential symmetry and/or asymmetry of basement features. The flow line design of this seismic survey is crucial in the North Atlantic Ocean where there is a ~30° change in spreading direction in Late Eocene times.

### 2.1. Acquisition and Processing

Acoustic energy was generated using a single generator-injector air gun with a total volume of 5.82 L (generator pulse = 4.1 L, injector pulse = 1.72 L) and a frequency bandwidth of 10–400 Hz. The air gun was towed at a depth of 5.5 m behind the vessel, which steamed at 2 m s<sup>-1</sup>. Shots were fired every 15 s (~30 m) with a chamber pressure of 20.7 MPa (i.e. 3,000 psi). Reflected acoustic energy was recorded on a 1,600 m long streamer towed at 7 m depth. This streamer consisted of 132 groups of hydrophones located every 12.5 m. Distance from the air gun to the first group (that is, near-trace offset) was 163 m. The digital sampling interval of recorded signals was 1 ms.

A typical processing sequence was used. Shot point gathers were assigned into common midpoint (CMP) gathers spaced every 6.25 m. Root-mean-square (rms) velocities were picked every 100 CMPs (i.e., every 6.25 m), followed by conventional stacking. A 12 Hz high-pass filter with a roll-off of 24 dB per octave was applied before stacking. Images were migrated using a poststack frequency-wave number (i.e., *f-k*) algorithm with a constant velocity of 1.5 km s<sup>-1</sup> (Stolt, 1978). Each profile was converted from two-way travel time to depth using smoothed interval velocities determined from picked rms velocities (typical velocities within sediment layer range from 1.6 to 2.5 km s<sup>-1</sup>). The resultant 21-fold stacked image has a vertical and horizontal resolution of 10–20 m. It is important to note that this resolution is sufficient to discriminate between kilometer-scale V-shaped ridges and the effects of pervasive normal faulting with displacements of tens to hundreds of meters.

### 2.2. Geologic Interpretation

The seismic profiles reveal the detailed structure of the Iceland and Irminger basins (Figure 4). The top of the oceanic basement is imaged beneath a pile of sediment that thickens away from the mid-ocean ridge. The sediment-basement interface is characterized by a high amplitude, uneven reflection that occurs beneath numerous weaker reflections from within the sediment pile. Reflections within the sediments are high frequency and define convex depositional geometries typical of the fine-grained contourite drift deposits found in the North Atlantic Ocean (Bianchi & McCave, 2000; Johnson & Schneider, 1969; Parnell-Turner et al., 2015). Sediments to the east of Reykjanes Ridge are typically more than twice as thick as sediments at a similar distance

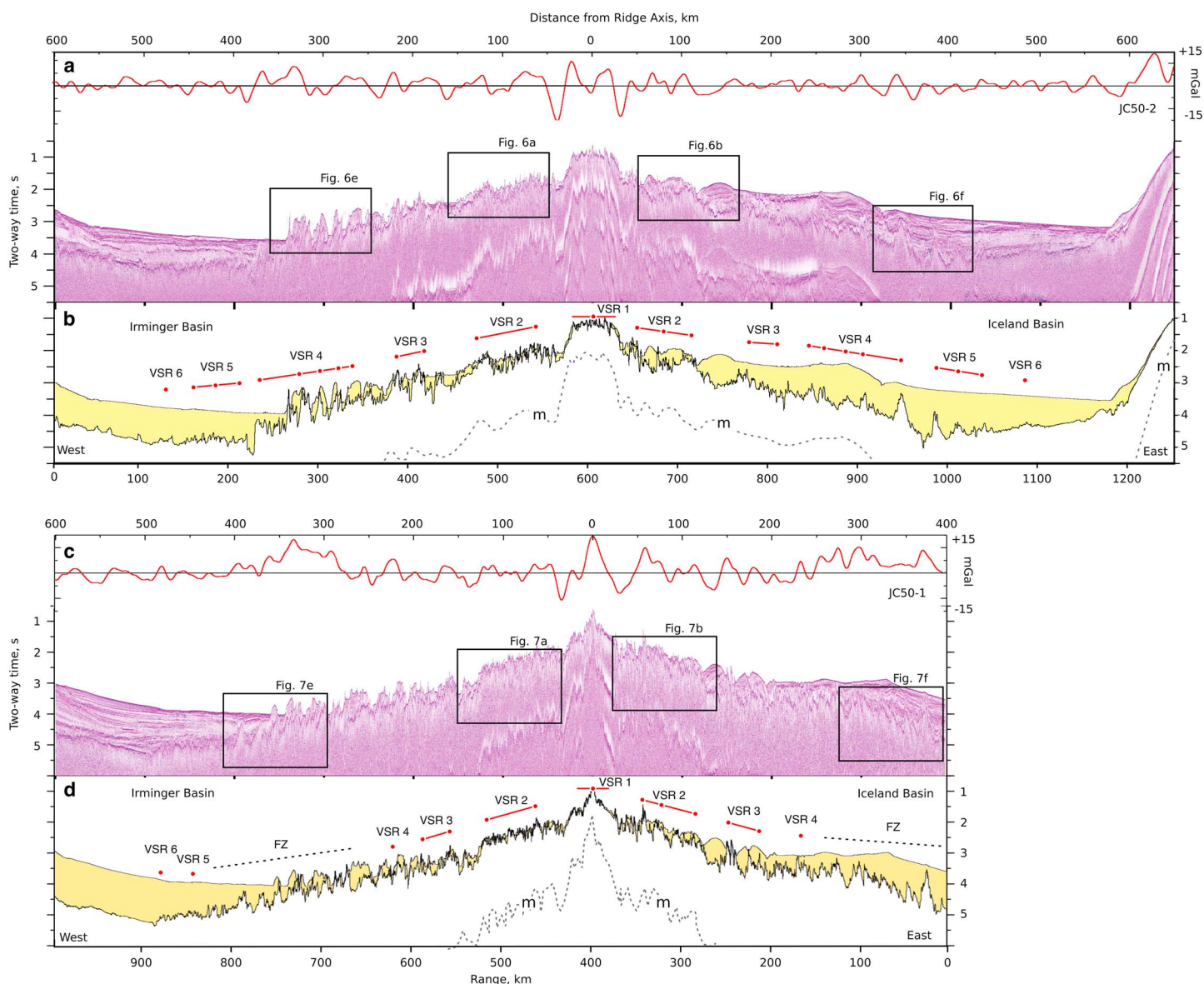


**Figure 4.** Time-migrated seismic reflection and gravity anomaly profiles, location shown in Figure 2. (a) JC50-2. Red lines = filtered free-air gravity anomaly (Sandwell et al., 2014). (b) Geologic interpretation. Solid lines = seabed and sediment-basement interface, yellow shading = sedimentary cover, labeled red dots/lines = VSRs/composite VSRs, dashed line = seabed multiple (m). (c) JC50-1. (b) Geologic interpretation.

from the axis on the western side (e.g., compare sediment thickness 200 km from ridge axis, Figure 4). These thick sediments are Gardar and Björn contourite drifts, which are deposited on the eastern flank of the Reykjanes Ridge bathymetric rise as deep-water flows southward through the Iceland Basin under the influence of the Coriolis force (Parnell-Turner et al., 2015).

### 2.2.1. Crustal Morphology

The Reykjanes Ridge itself is characterized by a central high on each of the four flow line profiles (Figure 5). On the northernmost profiles, JC50-2, JC50-3, and JC50-4, this central high consists of a ~42 km wide plateau which represents the youngest V-shaped ridge, VSR 1. This plateau is capped by a number of minor highs with elevations of up to 200 m which probably represent *en echelon* axial volcanic ridges (Parnell-Turner et al., 2013; Searle et al., 1998). On these three profiles, VSR 1 is flanked on either side by prominent bathymetric depressions, which are filled with sediments of up to 0.35 s two-way travel time (i.e., 200–300 m) thickness at a range of 90 km west of ridge axis (Figure 5g). On JC50-1 which is located ~200 km south of JC50-2, the central high is much narrower and sharper (Figure 5d). This profile crosses the leading edge of VSR 1, which is

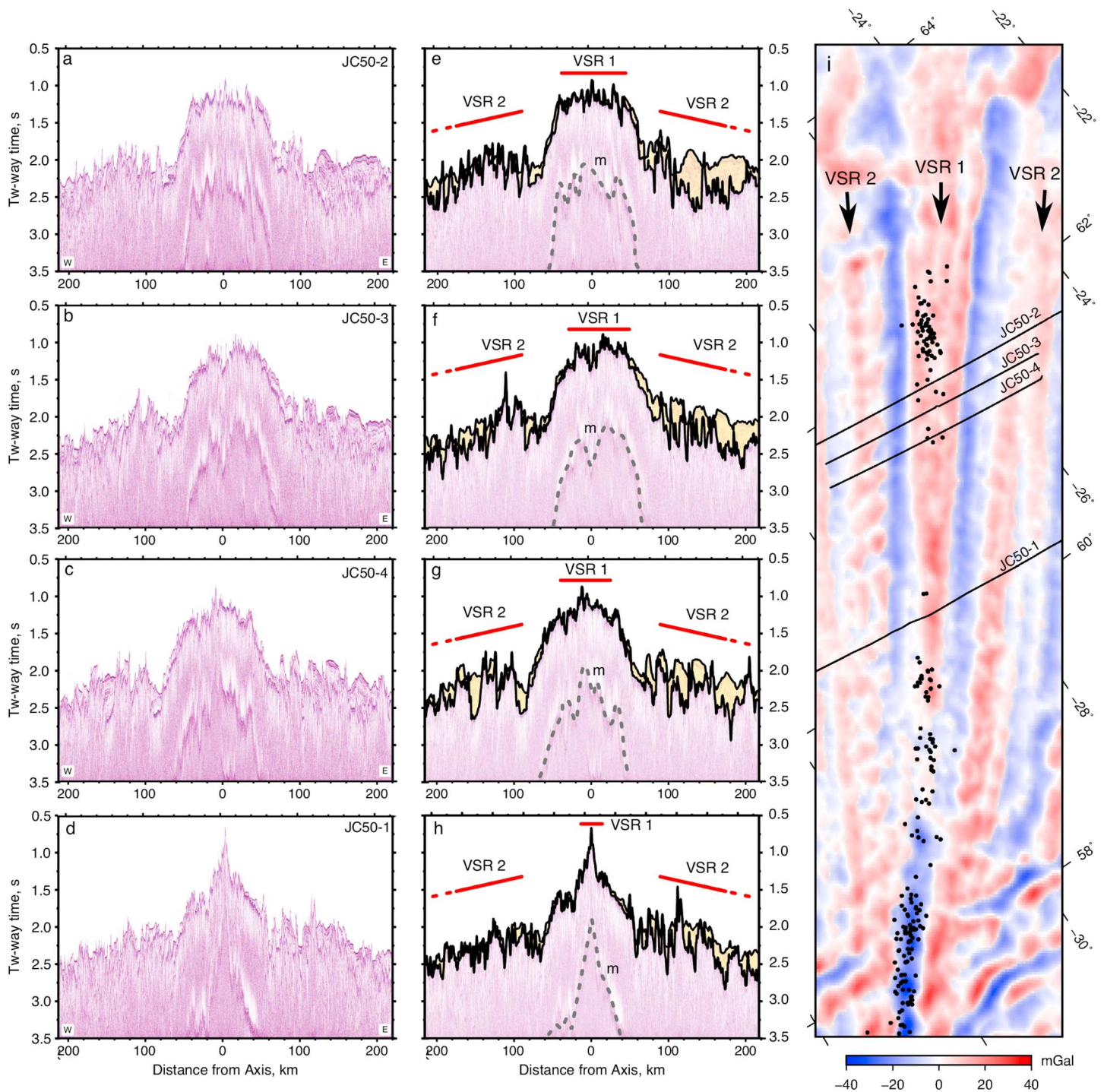


**Figure 5.** Detailed portions of seismic profiles crossing Reykjanes Ridge (see Figure 2 for location). (a–d) Profiles JC50-2, JC50-3, JC50-4, and JC50-1, respectively. (e–h) Geologic interpretation. Yellow shading = sedimentary cover, solid black lines = seabed and sediment-basement interface; labeled red lines = VSRs, m = seabed multiple. (i) Satellite free-air gravity anomaly map high-pass filtered to remove wavelengths >250 km (Sandwell et al., 2014). Labeled black lines = seismic profiles, black dots = relocated earthquakes between 1960 and 2009 ( $M_w > 4$ ; Engdahl et al., 1998); labeled arrows = VSRs.

not defined by a wide plateau. Instead, this edge has steeply dipping flanks, which give way to pronounced bathymetric depressions on either side.

Broadly symmetrical, long wavelength, highs and lows in the topography of the sediment-basement interface can be identified and mapped on JC50-1 and JC50-2. These ridges and troughs occur up to 550 km away

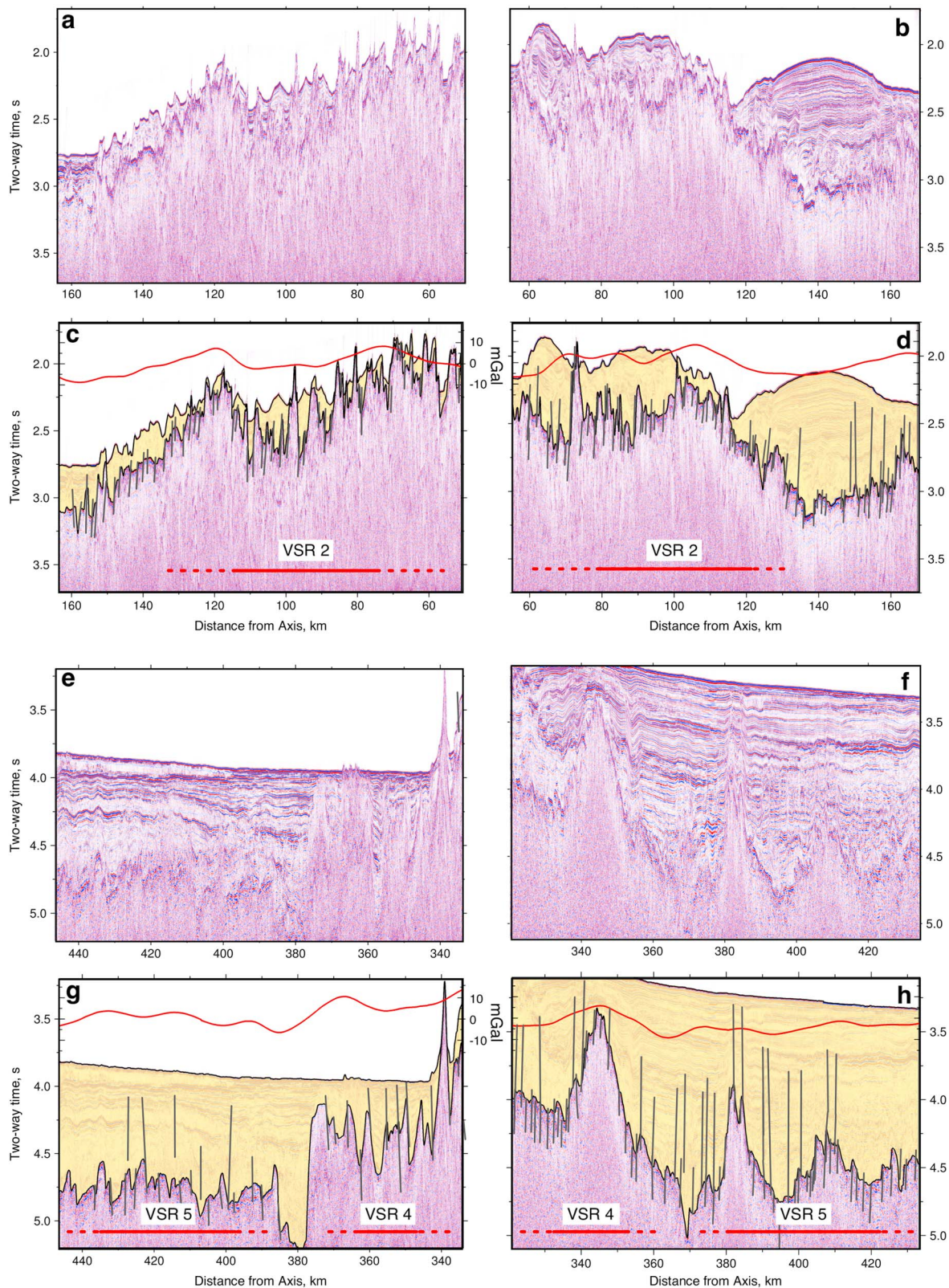


**Figure 6.** Detailed portions of seismic profiles from JC50-2 (see Figure 4 for location). (a and b) Young V-shaped ridges located ~100 km west and east of Reykjanes Ridge, respectively. (c and d) Geologic interpretation. Yellow shading = sedimentary cover, solid black lines = seabed and sediment-basement interface, subvertical solid lines = normal faults, labeled red lines = VSRs, red lines = filtered free-air gravity anomalies (Sandwell et al., 2014). (e and f) Older V-shaped ridges located ~320 km west and east of Reykjanes Ridge, respectively. (g and h) Geologic interpretation.



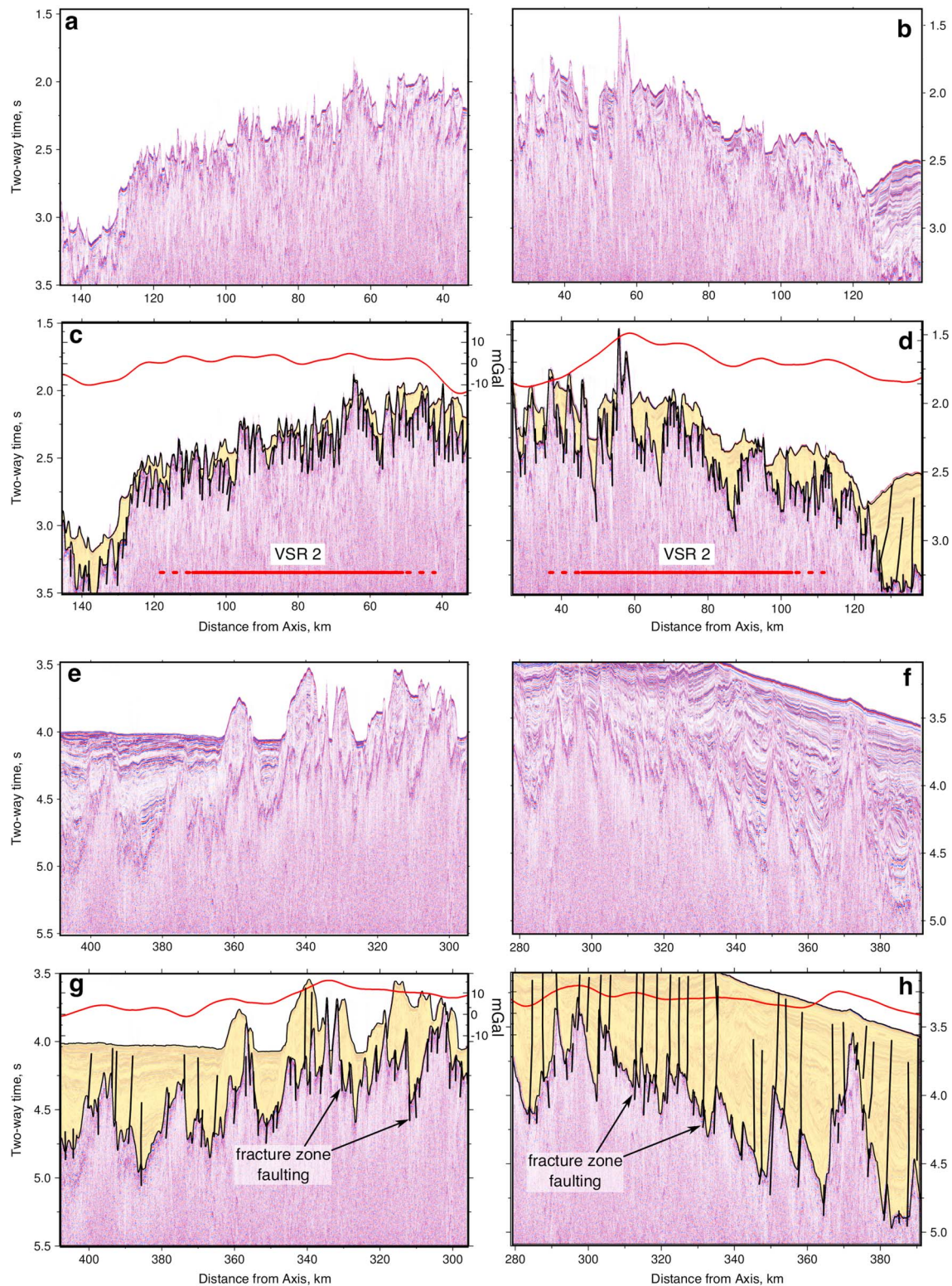


**Figure 7.** Detailed portions of seismic profiles from JC50-1 (see Figure 4 for location). (a and b) Young V-shaped ridges located ~100 km west and east of Reykjanes Ridge, respectively. (c and d) Geologic interpretation. Yellow shading = sedimentary cover, solid black lines = seabed and sediment-basement interface, subvertical solid lines = normal faults, labeled red lines = VSRs, red lines = filtered free-air gravity anomalies (Sandwell et al., 2014). (e and f) Older V-shaped ridges located ~350 km west and east of Reykjanes Ridge, respectively. (g and h) Geologic interpretation.

from the mid-oceanic ridge and coincide with positive and negative free-air gravity anomalies (Figure 4). The ridges are 15–70 km wide, up to ~750 m high, and are broken up, but not defined, by numerous high-angle normal faults. These faults are typically spaced 1–5 km apart (Figure 6d). Conjugate pairs of V-shaped ridge with similar amplitudes and wavelengths can be identified on either side of the Reykjanes Ridge (Figures 6 and 7). VSR 2 consists of two basement highs that are 60–80 km wide, up to 2.25 km high on JC50-2, and more pronounced on the western flank (Figures 6c and 6d). On JC50-1, VSR 2 consists of a single 80 km wide high that is broadly symmetrical about the ridge axis (Figures 7c and 7d).

Significantly, buried V-shaped ridges are clearly imaged beneath thick sedimentary cover on older Paleogene oceanic crust. These ridges have different morphologies and amplitudes on either side of the spreading axis. For example, VSR 4 consists of a series of four faulted basement highs on JC50-2 to the west of the Reykjanes Ridge, each of which is 400–500 m high at a range of 360 km from axis (Figure 6g). East of Reykjanes Ridge on the same profile, VSR 4 is a distinctive peak that is 750 m high at a range of 345 km from axis (Figure 6h). These older VSRs are generally asymmetric with steep sides that face toward the mid-oceanic ridge. In contrast, JC50-1 crosses a zone of intense fracturing, where VSRs appear to be absent on satellite gravity imagery (Figures 7g and 7h). At these ranges on both flanks, pervasive faulting occurs and long-wavelength basement highs are not easily identifiable.

Numerous fault-bounded blocks can be identified on the seismic reflection profiles. The clearest examples occur at a range of 340–360 km from the ridge axis on JC50-2 and at 300–400 km on JC50-1 (Figures 6g and 7g, respectively). Three characteristics enable fault-bounded blocks to be distinguished from VSRs. First, fault blocks are typically 1–5 km in width and are bounded by steeply dipping faults with throws of 100–300 m. In contrast, VSRs are typically 15–70 km wide with amplitudes of 1 km (e.g., Figure 6h). Normal faults often dissect but do not define VSRs. In other words, these faults have throws of several hundreds of meters that are minor compared with the scale of a given VSR. Second, stratigraphic growth within fault-bounded blocks is commonly observed (e.g., at a range of 380 km on Figure 7f). Such growth is generally less evident on the flanks of VSRs. Third, fault-bounded blocks are often asymmetric, dipping away from the mid-oceanic ridge. In contrast, many VSRs are broadly symmetric features that are superimposed upon a smooth age-depth trend.

### 2.2.2. Plate Spreading Mode

At slow spreading ridges, plate separation is accommodated through a combination of magmatic accretion and normal faulting. Magmatism is typically focused within a 5–10 km neovolcanic zone at the ridge axis with active normal faulting localized on either side of the neovolcanic zone (e.g., Behn & Ito, 2008; Macdonald et al., 1988). Here we have investigated the contribution that normal faulting makes by measuring the cumulative horizontal displacement at the sediment-basement interface along profiles JC50-1 and JC50-2 (Figure 8).

The depth-converted sediment-basement interface was mapped across hanging wall and footwall blocks and used to calculate the length of each fault-bounded block in the flow line direction. The amount of horizontal extension (i.e., heave) accommodated by an individual fault-bounded block was estimated by dividing the present-day distance between adjacent block crests by the original block width which allows for rigid block rotation. In this way, the cumulative heave across many fault-bounded blocks can be measured as a function of distance from ridge axis (Figure 8b).

Cumulative heave can be used to gauge how the amount of accommodation by brittle faulting varies through space and time. Along JC50-2, cumulative heave steadily increases as a function of distance to yield total horizontal extensions of 30 km and 40 km at the respective eastern and western ends of this profile. Along JC50-1, larger values of 50 and 55 km were obtained. The changing rate of brittle (i.e., tectonic) accommodation is estimated from the gradient of the cumulative heave. Along JC50-2, the average rate is ~0.05 (Figure 8b). In contrast, JC50-1 shows two distinct regimes with different amounts of brittle accommodation. Within 150 km either side of the mid-oceanic ridge, the average rate is similar to that along JC50-2. At ranges of 150–400 km, this rate increases by a factor of 3. At ranges of greater than 400 km, the rate drops back to values comparable to those along JC50-2.

We can use these estimates of the rate of brittle accommodation to infer the rate of magmatic accretion,  $M$ , which is defined as the difference between the total spreading rate and the rate of brittle accommodation (Behn & Ito, 2008; Buck et al., 2005). We calculated time-averaged estimates of  $M$  as a function of distance along each flow line within a running 50 km wide window that is equivalent to a time interval of 4 Ma

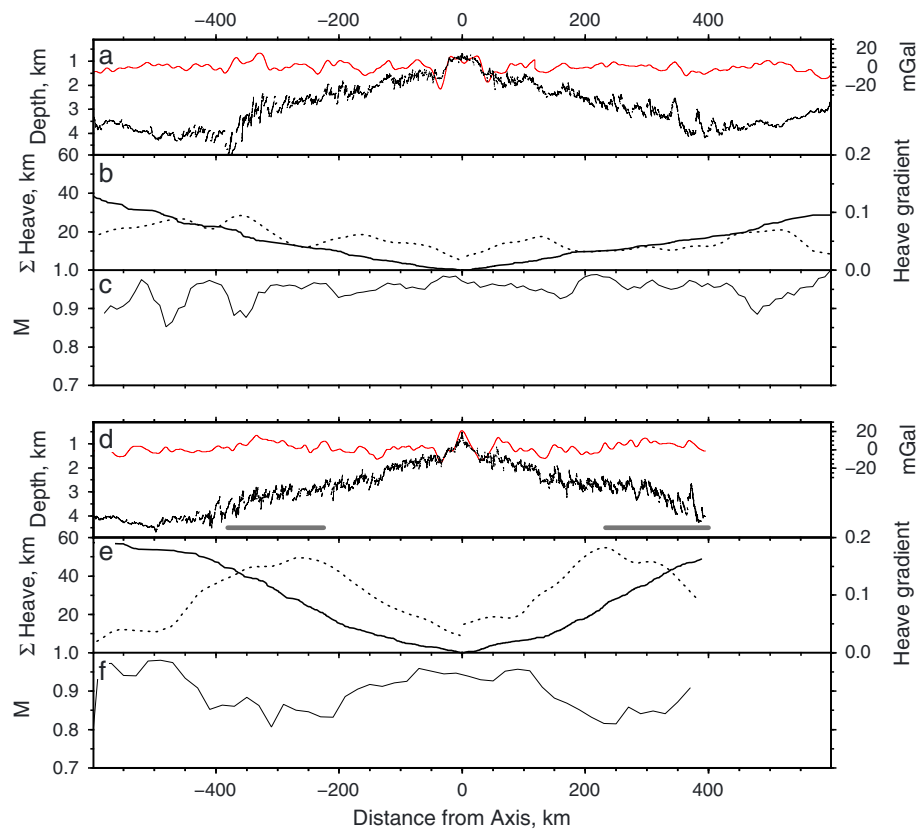


**Figure 8.** Fault analysis of JC50-2 and JC50-1. (a) Analysis of JC50-2. Red line = filtered free-air gravity anomaly (Sandwell et al., 2014); black lines = fault-bounded block geometry. (b) Solid line = cumulative heave (i.e., horizontal displacement) as function of distance; dashed line = gradient of cumulative heave as function of distance. (c) Estimate of magmatic fraction of plate separation,  $M$ , as function of distance. (d) Analysis of JC50-1. Red line = free-air gravity anomaly, black lines = fault-bounded block geometry, horizontal gray bars = timing of lobes of fractured oceanic crust. (e) Solid line = cumulative heave as function of distance; dashed line = gradient of cumulative heave as function of distance. (f) Estimate of magmatic fraction of plate separation,  $M$ , as function of distance.

for a spreading rate of  $1.25 \text{ cm yr}^{-1}$  (Figure 8b). This time interval was chosen to minimize the effects of local variations in crustal accretion. Along JC50-2,  $M$  varies between 0.9 and  $\sim 1$  within 300 km on either side of the ridge axis. These values indicate that magmatic accretion accounts for the bulk of plate spreading during Neogene times. An interval of reduced  $M$  occurs at a range of 375 km on the western flank of JC50-2. It is not apparent on the eastern flank, which means that it is difficult to explain in terms of a plate reorganization event. A second interval of reduced  $M$  occurs at a range of 475 km on both flanks, which corresponds to a significant change in plate spreading azimuth that took place after chron 20 at 43 Ma (Smallwood & White, 2002). This reorganization appears to have coincided with a reduction in the proportion of spreading accommodated by magmatic accretion. Along JC50-2,  $M$  is  $>0.9$  within 175 km on either side of the ridge axis.  $M$  reduces to  $\sim 0.85$  at ranges of 175–400 km.

These changes in the proportion of brittle and magmatic accommodation correlate with lobate zones of rugose oceanic crust characterized by fracture zones. Symmetric zones are thought to have formed during a period when the planform of the plume was dramatically reduced (Jones, White, & Maclennan, 2002, Parnell-Turner et al., 2014; White, 1997). At ranges of  $>400$  km on JC50-1, magmatic accretion is inferred to have been dominant since  $M > 0.9$ . This dominance correlates with morphologically smooth oceanic crust devoid of fracturing that may have been generated when the planform of the plume extended much further south (White, 1997). The relatively constant value of  $M$  along JC50-1 implies that the plate reorganization event at 43 Ma had less influence at distances closer to the center of the plume on Iceland, since crustal accretion was probably dominated by the presence of the plume head beneath the ridge axis.

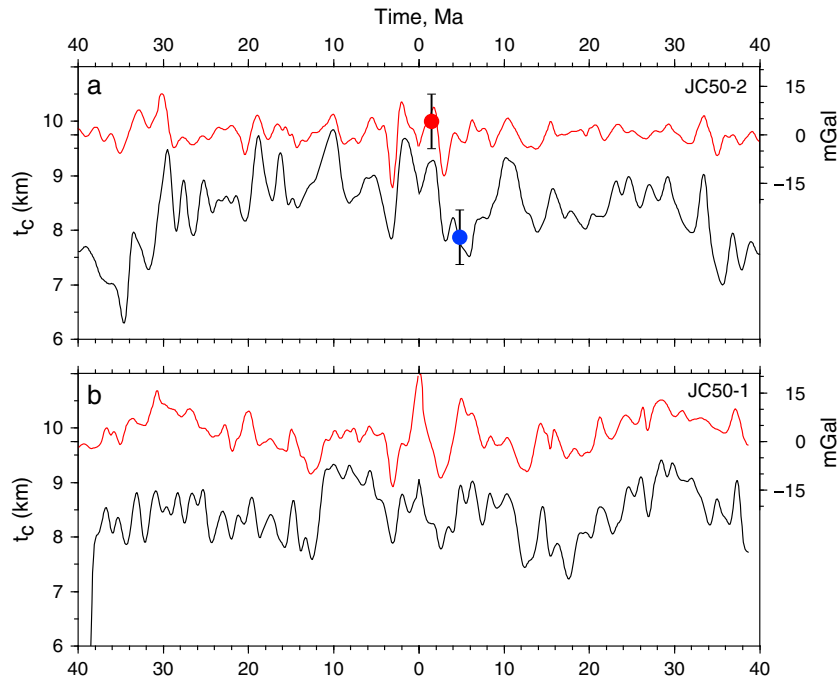


**Figure 9.** Estimates of crustal thickness,  $t_c$ , determined from residual depth analysis of seismic profiles. (a) JC50-2. Black line = estimated  $t_c$  as function of geologic time; red line = filtered free-air gravity anomalies (Sandwell et al., 2014), red/blue circles = crustal thickness measurements from seismic refraction experiment (Smallwood & White, 1998). (b) JC50-1.

Unsurprisingly, V-shaped ridge activity appears to correlate with the long-wavelength lobate pattern and with the cumulative rate of magmatic accretion (Figure 8f). This observation is consistent with the results of Parnell-Turner et al. (2013) from the Reykjanes Ridge, where there is a positive correlation between growth of the youngest V-shaped ridge, magmatic accretion, and absence of brittle normal faulting.

### 2.3. Crustal Thickness and Temperature Estimates

It is generally recognized that oceanic crust is generated by decompression melting of dry mantle peridotite at the ridge axis (e.g., McKenzie & Bickle, 1988; White et al., 1992). An important corollary is that measurements of oceanic crustal thickness can be used as a proxy for asthenospheric temperature in the geologic record. In the North Atlantic Ocean, there are relatively few modern estimates of crustal thickness. Since the seismic reflection profiles presented here were not designed to image the base of the crust, we use residual depth measurements of the sediment-basement interface to gauge crustal thickness variation along each flow line. Residual depth,  $d_r$ , is the difference between the present-day water-loaded depth to basement, which is calculated by correcting for sedimentary loading, and the depth predicted by assuming an age-depth relationship (Parsons & Sclater, 1977). At short wavelengths, residual depth anomalies can be accounted for by local changes in oceanic crustal thickness. In the vicinity of the plume, the reference crustal thickness is  $t_c = 8.4$  km (Smallwood & White, 1998). Therefore, positive and negative residual depth anomalies (and their associated free-air gravity anomalies) are indicative of crust that is respectively thicker and thinner than this reference value (Figure 9; Appendix A). Within 400 km of the Reykjanes Ridge, crustal thickness varies by  $\pm 1.5$  km between V-shaped ridges and troughs. This variation is consistent with two estimates of crustal thickness made from the seismic wide-angle experiments of Smallwood and White (1998).

If crust is generated at the mid-ocean ridge by isentropic decompression of anhydrous mantle, the asthenospheric potential temperature,  $T_p$ , can be estimated from residual depth measurements using an approximate form of the melting model originally described by White et al. (1995) where

$$T_p \approx 16 \left[ t_c + \left( \frac{\rho_a - \rho_w}{\rho_a - \rho_c} \right) d_r \right] + 1,200. \quad (1)$$

In this equation,  $\rho_a = 3.2 \text{ Mg m}^{-3}$  is density of asthenospheric mantle,  $\rho_c = 2.8 \text{ Mg m}^{-3}$  is density of oceanic crust, and  $\rho_w = 1.0 \text{ Mg m}^{-3}$  is the density of sea water.

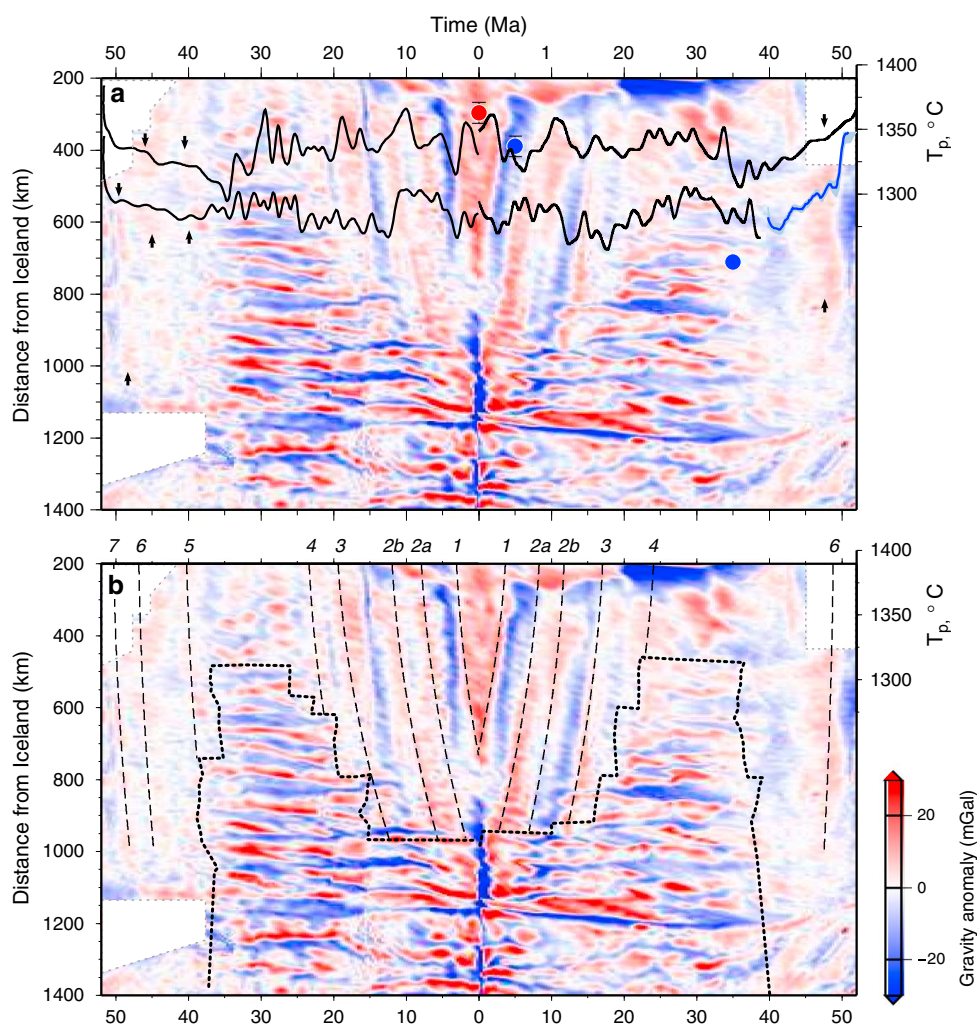


**Figure 10.** Chronology of transient mantle plume activity. (a) Map of gravity anomalies as function of crustal age and distance from plume center (i.e., 63.95°N, 17.4°W; Shorttle et al. (2010)). Black lines = potential temperature,  $T_p$ , calculated from residual depth profiles, blue lines with band =  $T_p$  calculated from wide-angle seismic refraction data (Parkin & White, 2008), red/blue circles =  $T_p$  calculated from crustal thickness measurements (Smallwood & White, 1998; Whitmarsh, 1971), black arrows = weak linear gravity anomalies. (b) Map of gravity anomalies as before. Numbered dashed lines = best fit V-shaped ridges calculated using radial asthenospheric flow, dotted line = demarcation of smooth-rough transition gauged from magnetic picks (Parnell-Turner et al., 2014).

Estimates of  $T_p$  are combined with satellite gravity observations and projected into age-distance space (Figure 10). There is broad agreement between the inferred variation of  $T_p$  along each flow line and the pattern of positive and negative gravity anomalies for oceanic crust that is <20 Ma and >40 Ma. At the Reykjanes Ridge axis itself, the youngest V-shaped ridge, VSR 1, is starting to unzip from the north. It is generated by an asthenospheric temperature anomaly of  $\sim 25^\circ\text{C}$  that is consistent with a single modern crustal thickness measurement of  $10.4 \pm 0.5$  km (Smallwood & White, 1998). The presence of a thermal anomaly of this magnitude is consistent with the subplate temperature calculated by inverting geochemical analyses of dredged basalts along the Reykjanes Ridge, with a marked gap in earthquake seismicity where VSR 1 intersects the ridge, and with the changing spatial density of normal faulting and volcanic seamounts (Parnell-Turner et al., 2013; Poore et al., 2011). Rheologic modeling suggests that these disparate observations can be quantitatively linked by a thermally triggered decrease in the thickness of the brittle seismogenic layer.

VSR 1 is flanked on either side by a well-defined pair of troughs where the projected crustal thickness is  $8.6 \pm 0.5$  km. VSR 2 is a compound ridge that can be divided into at least two discontinuous strands which do not exhibit symmetry on either side of the mid-oceanic ridge. It is in turn flanked by a symmetric pair of troughs which in turn are flanked by two sets of less well defined V-shaped ridges, VSR 3 and VSR 4.

VSRs 2a and 2b represent  $T_p$  anomalies of  $\sim 25^\circ\text{C}$ , while collective VSRs 3 and 4 are probably generated by smaller thermal anomalies of  $\sim 10\text{--}15^\circ\text{C}$ . The oldest V-shaped ridges that constitute part of VSRs 4 are particularly prominent on the eastern side of JC50-2 at ranges of 300–450 km. These ridges mark the start of thermal perturbations associated with the modern (i.e., Neogene) plume.

On Figure 10, two prominent and approximately symmetric lobes of fractured crust with discontinuous magnetic anomalies are visible south of Iceland. A single vintage crustal thickness measurement of 6.1 km suggests that these lobes represent a period of time between approximately 40 and 20 Ma when the plume was cooler and therefore reduced in size (Whitmarsh, 1971). This observation suggests that the rough-smooth boundary is a useful proxy for the lateral extent of the plume as a function of time. On oceanic floor that is older than  $\sim 40$  Ma, basement appears to be smooth and free of fracture zones. This morphology is similar to that of the youngest seafloor adjacent to ridge axis where prominent V-shaped ridges and troughs occur (Figure 10). It probably represents a period of time when the planform of the plume extended out to radial distances of more than 1,000 km (Jones, 2003; White, 1997). As it happens, JC50-1 and JC50-2 straddle the northern limit of these lobes of fractured crust. On JC50-1, there is clear evidence for well-defined fault-bounded blocks at a range of 300–400 km. These blocks just fall inside the lobate regions. On JC50-2, a series of well-defined V-shaped ridges appear to be visible at a similar range.

Weak north-south linear gravity anomalies can be traced on oceanic crust as old as 50 Ma along both margins over radial distances of hundreds of kilometers (Figure 10a). We acknowledge that these anomalies are at least partly generated by bathymetric variations associated with contourite drift deposits (e.g., Maury Drift at a range of  $\sim 1,200$  km). Nevertheless, we provisionally identify three of these features as V-shaped ridges (VSRs 5–7). Significantly, VSR 6 coincides with a change in oceanic crustal thickness identified by a wide-angle seismic refraction experiment, which is consistent with an asthenospheric temperature anomaly of  $\sim 15^\circ\text{C}$  (Figure 10; Parkin & White, 2008). Residual depth anomalies associated with VSRs 5–7 have a similar size and coincide with weak linear gravity anomalies. We suggest that these anomalies represent temperature fluctuations within the head of a rapidly shrinking and cooling plume.

Finally, we emphasize the importance of restricting residual depth analysis to regions unaffected by fracture zones, which are delineated using magnetic anomalies. Seafloor transected by fracture zones is characterized by discontinuous and offset magnetic anomalies (Figure 2b). We identify this fractured region using magnetic anomaly picks from Jones, White, & MacLennan (2002) which are then projected into age-distance space (Figure 10a). South of this region, the relationship between  $T_p$  from residual depth profiles and gravity anomalies is not straightforward, and the absence of clearly defined V-shaped ridges suggests that plume-driven thermal perturbations may not have flowed beneath the lithospheric plates during this time interval.

### 3. North Atlantic Igneous Province

This contribution is principally focussed on the structure and composition of oceanic crust formed at a mid-oceanic ridge that bisects the Iceland plume. Here we broaden the scope of this analysis by considering Cenozoic igneous activity throughout the North Atlantic region (e.g., Geikie, 1889; Saunders et al., 1997; White & McKenzie, 1989). Early Cenozoic continental breakup coincided with extensive magmatism that led to formation of the North Atlantic Igneous Province (NAIP). The first phase of volcanism commenced at 61–62 Ma and reached from Baffin Island and west Greenland in the northwest to the British Isles in the southeast (Saunders et al., 1997). A second phase commenced at 56 Ma and included ubiquitous seaward dipping reflections along adjacent continental margins, the Main Series of basalts in eastern Greenland, and magmatic activity along the Greenland-Scotland Ridge and on Iceland (Saunders et al., 1997). These coeval and widespread phases of volcanism are widely considered to be associated with the evolution of the Iceland plume. However, it is less clear if subsequent igneous activity can also be attributed to plume activity (Breivik et al., 2006; Larsen et al., 1992; Saunders et al., 1997; Storey et al., 1998, 2007; Tegner et al., 1998; White & McKenzie, 1989; Wilkinson et al., 2016). Here we examine the extent to which this later activity coincides with the V-shaped ridge chronology.

#### 3.1. Postbreakup Basaltic Magmatism

Wilkinson et al. (2016) compiled a database that summarizes the chronology of igneous rocks from the NAIP. In order to identify potential plume-related volcanism, we select a subset of extrusive high MgO samples from this database, ignoring intrusive lithologies which probably underwent fractional crystallization (i.e., granites,

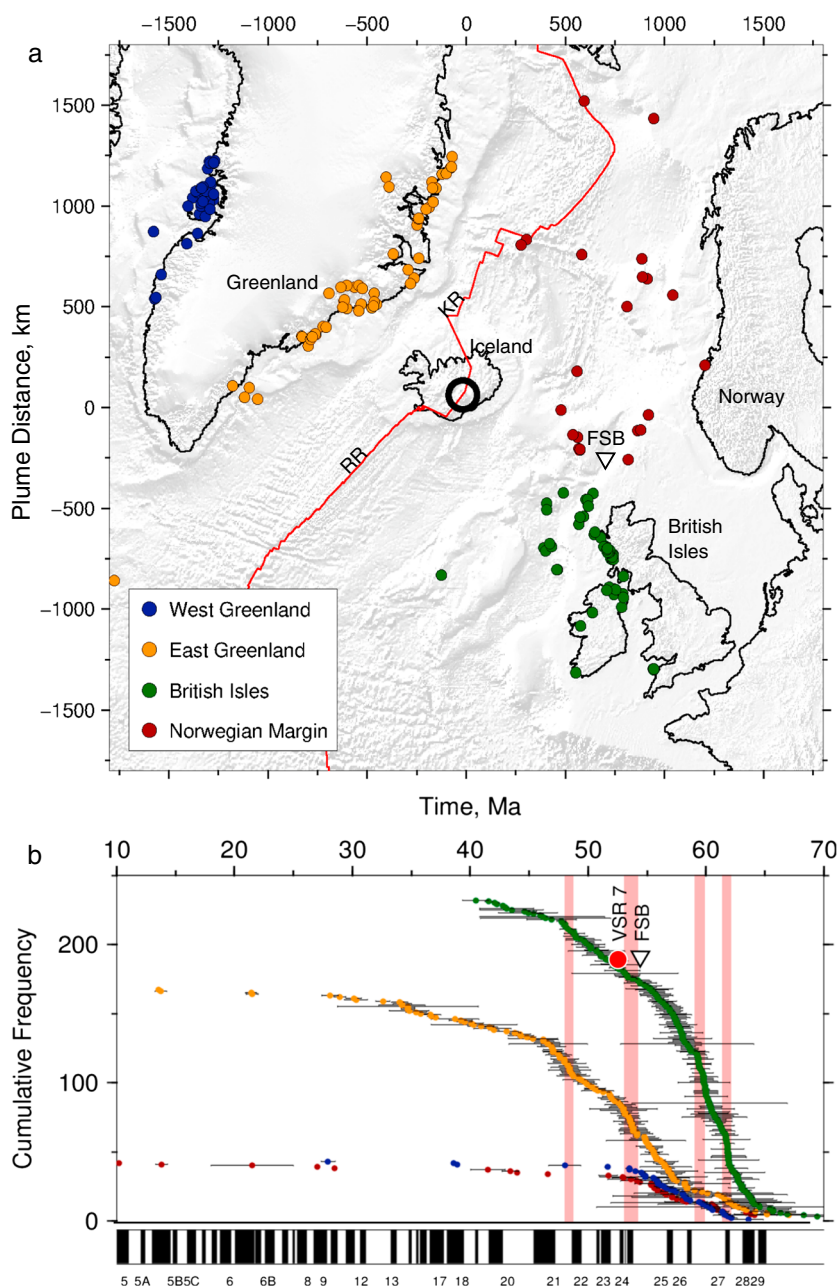


**Figure 11.** (a) Bathymetric map of North Atlantic Ocean (Cartesian projection centered on Iceland plume and illuminated from northwest) that shows distribution of dated extrusive igneous rocks (Wilkinson et al., 2016). Colored circles = dated igneous rocks, red line = mid-oceanic ridge, open circle = center of plume, inverted triangle = location of regional 55 Ma unconformity surface (Shaw Champion et al., 2008), FSB = Faroe-Shetland Basin, RR = Reykjanes Ridge, KR = Kolbeinsey Ridge. (b) Cumulative frequency of dated igneous rocks as function of geologic time where horizontal bars are equal to  $2\sigma$  from Wilkinson et al. (2016); colored circles as before; pink bands = inferred episodes of increased magmatic activity, red circle = inferred age of VSR 7, inverted triangle = 55 Ma unconformity surface shown in Figure 11a.

syenites, and gabbros). Locations of rocks from this subset are shown according to their present-day distance from the putative center of the plume (Figure 11a). They are divided into four subprovinces (i.e., west Greenland, east Greenland, British Isles, and Norwegian margin), and a cumulative frequency diagram is used to identify periods of increased volcanic activity (Figure 11b). This comprehensive database is a useful representation of known samples, but we acknowledge that inherent nonsystematic sample distribution may result in temporal and spatial biases that cannot easily be addressed.

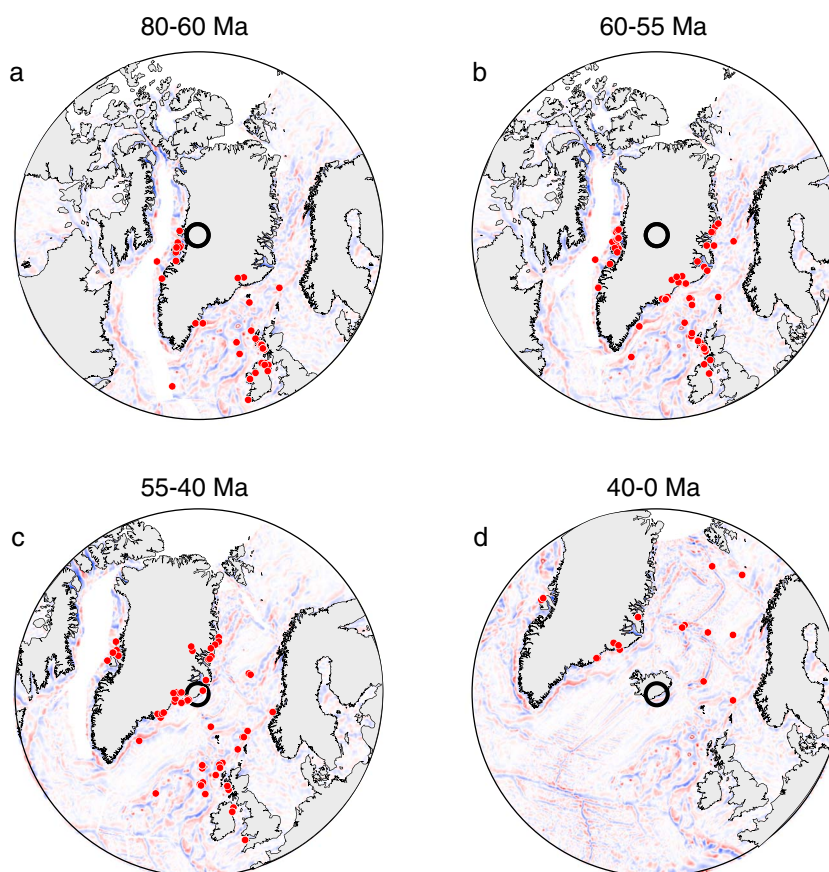


**Figure 12.** Series of plate reconstructions centered on position of plume that show high-pass filtered free-air gravity anomalies with wavelengths  $>250$  km and distribution of igneous activity (Gnomonic projection centered on  $63.95^{\circ}\text{N}$ ,  $17.4^{\circ}\text{W}$ ). (a) Interval of 80–60 Ma. Red circles = distribution of igneous rocks for this time interval; open circle = center of plume; plate reconstruction for 60 Ma calculated using GPlates software package with appropriate rotation poles (Seton et al., 2012). (b) Interval of 60–55 Ma. Plate reconstruction calculated for 55 Ma. (c) Interval of 55–40 Ma. Plate reconstruction calculated for 40 Ma showing development of VSRs on oceanic crust. (d) Interval of 40–0 Ma. Present-day plate configuration.

There are four distinct phases of increased volcanism approximately centered on 62, 59, 54, and  $48 (\pm 0.5)$  Ma that straddle the onset of seafloor spreading at  $\sim 54$  Ma. The timing of each phase is obtained from changes in slope on Figure 11b. The burst of activity at 54 Ma itself is coeval with the formation of VSR 7 and with regional uplift and erosion of Paleocene marine deposits on the southeastern edge of the Faroe-Shetland basin (Figure 11b; Shaw Champion et al., 2008; Hartley et al., 2011). These phases of activity occur every 3–4 Ma, which appears to broadly reflect the time-dependent plume behavior determined from a V-shaped ridge chronology. It is consistent with the most significant episodes of clastic deep-water fan deposition on either side of the British Isles (White & Lovell, 1997). Younger phases of volcanism occurred at  $\sim 30$ – $36$  Ma in east Greenland,  $\sim 39$  Ma and  $\sim 28$  Ma in west Greenland, and  $\sim 44$  Ma in the British Isles (Figure 11b). Along the Norwegian margin, volcanism occurred at  $\sim 42$  Ma,  $\sim 28$  Ma, and 10 Ma.

A series of plate reconstructions help to gauge the spatial and temporal distribution of magmatism during different periods (Figure 12). Reconstructions for 80–60 and 60–55 Ma reveal how syn-rift magmatism is regionally distributed, reflecting the substantial planform of the plume during Paleogene times (Figure 12).

The 55–40 Ma period marks onset of seafloor spreading in the North Atlantic ocean, coinciding with the appearance of weakly defined V-shaped ridges that reflect small temperature fluctuations within the head of a rapidly shrinking plume (Figure 12c). During this period, minor igneous activity occurred in west Greenland: a basaltic dyke was intruded on Disko Island at 53.6 Ma, a dyke was intruded on the Nuussuaq peninsula at 48 Ma, and a lamprophyre dyke was intruded in Godthåbsfjord at 51.8 Ma (Larsen et al., 2009, 2016; Storey et al., 1998). These intrusions are coeval with more abundant volcanism in east Greenland (e.g., Larsen et al., 2013;



Nevle et al., 1994; Tegner et al., 2008). On the conjugate margin, basaltic volcanism occurred on the Anton Dohrn seamount at 41.3 Ma, a basaltic dyke was intruded on Lewis north of Scotland at 45.2 Ma, and the top of the Antrim Lava Group erupted at 49.9 Ma (Faithfull et al., 2012; Ganerød et al., 2010; O'Connor et al., 2000).

A significant hiatus in volcanic activity is evident between 40 and 30 Ma which coincides with wholesale shrinking of the plume. The youngest volcanism of the North Atlantic region is largely distributed in quadrants northeast of Iceland (e.g., east Greenland, Jan Mayen, and Norwegian Sea; Figure 12d). In east Greenland, lavas of the Vindtop Formation are extruded at 13.6 Ma and an alkaline sill is intruded on Hvalrosø at 20.3 Ma (Larsen et al., 2014; Storey et al., 2004). In west Greenland, a basaltic dyke on Ubekendt Ejland at 34.1 Ma and a tuff on Hareøen at 28.3 Ma represent the final stages of volcanism (Larsen et al., 2016; Storey et al., 1998).

Youthful volcanism across Greenland cannot easily be ascribed to breakup of the Labrador Sea, where the youngest identifiable magnetic anomaly is chron 21 (46 Ma), after which any spreading is amagmatic (Roest & Srivastava, 1989). Instead, it is more likely that late stage magmatism is caused by transient activity of the plume. A combination of residual depth measurements, long-wavelength free-air gravity anomalies, and full-waveform seismic tomographic inverse modeling suggest that the present-day planform of the plume is highly irregular (Figure 1; Davis et al., 2012; Rickers et al., 2013). A series of finger-like protrusions reach beneath Greenland, beneath the northwest European shelf, and beneath different portions of the adjacent oceanic basins. Schoonman et al. (2017) suggest that these semiregular horizontal protrusions of asthenosphere are a large-scale manifestation of the classic Saffman-Taylor fluid dynamical instability whereby a less viscous fluid is injected into a more viscous surrounding. The resultant radial and miscible viscous fingers are probably hot and may have given rise to sporadic igneous activity.

#### 4. Discussion

In the light of the regional seismic reflection profiles presented here, we wish to evaluate three competing hypotheses that have been proposed to account for V-shaped ridge activity in the North Atlantic Ocean. First, Briais and Rabinowicz (2002) followed by Hey et al. (2010), Benediktsdóttir et al. (2012), and Hey et al. (2016) propose that V-shaped ridges are essentially pseudofaults that are generated by rift propagation. In this hypothesis, VSRs are generated by local tectonic reorganization and have negligible thermal significance. Second, Martinez and Hey (2017) proposed that V-shaped ridges are generated by shallow buoyant instabilities that initiate beneath Iceland and propagate along the linear subaxial melting zone beneath the Reykjanes Ridge. In this scheme, it is envisaged that patches of damp melting propagate down the axis, although rapid horizontal flow is specifically not implied. Martinez and Hey, 2017's (2017) qualitative proposal is similar in many respects to a previously published model (Murton et al., 2002). Third, Vogt (1971), Ito (2001), Jones, White, & MacLennan (2002), and numerous subsequent contributions argue that diachronous V-shaped ridges are generated when thermal anomalies are advected away from the center of the plume. Figure 3 illustrates each of these competing hypotheses.

##### 4.1. Propagating Rifts

Hey et al. (2010) and Benediktsdóttir et al. (2012) report compelling evidence for asymmetric accretion along the Reykjanes Ridge. They suggest that this asymmetry is produced by a series of propagating rifts. In their model, bathymetric depressions associated with negative gravity anomalies, which we refer to as V-shaped troughs, are interpreted as pseudofault scarps that converge into southward propagating rift tips at the ridge axis.

The model relies upon the existence of small-offset transform faults that are not easily identifiable along the Reykjanes Ridge (Figure 3a). These transform faults are progressively eliminated by propagating rifts which gives rise to a region of smoother morphology unaffected by present-day fracture zones. In this way, regions where VSRs now exist are hypothesized to have been originally transected by fracture zones. This interpretation is in obvious contrast with thermal models which postulate that the difference between smooth and fractured oceanic seafloor is a direct consequence of the presence or absence of hot plume head material beneath the ridge axis at the time of crustal formation (Jones & White, 2003; White, 1997). These models suggest that during episodes of increased plume activity, the planform of the plume expands and the horizontal advection of minor thermal instabilities produces VSRs on both flanks of the ridge axis at distances of up to 1,000 km from the center of the plume on Iceland. During episodes of reduced plume activity, this planform shrinks, cooler crust with fracture zones is generated, and V-shaped ridges are absent. Crucially, the difference

between the fabric of smooth and fractured seafloor reflects the primary mechanism of accretion as opposed to subsequent modification by propagating rifts.

#### 4.1.1. Off-Axis Volcanism, Oceanic Gateways, and Transient Epeirogeny

We suggest that the propagating rift hypothesis is exclusively an on-axis process with few off-axis consequences. Nevertheless, there is evidence for off-axis volcanism in the vicinity of the plume and for regional epeirogeny that affected Greenland-Scotland Ridge. These disparate observations have significant implications for any hypothesis of V-shaped ridge generation.

Walters et al. (2013) present geochemical analyses from the abandoned Húnaflói rift zone near Skagi in northern Iceland. Here spreading ceased at 7–4 Ma but field observations show that renewed melting occurred at this abandoned rift zone between ~3 Ma and 1 Ma. Up to 400 m thickness of tholeiitic basalts accumulated before the rift zone once more became extinct. A thermal and mechanical melting model suggests that the timing, composition, and volume of renewed melting can be accounted for by a pulse of anomalously hot asthenosphere that advected horizontally within the plume head. This pulse traveled beneath the Húnaflói rift zone at ~3 Ma (Walters et al., 2013).

There is evidence for renewed off-axis melting throughout the wider North Atlantic Igneous Province (Wilkinson et al., 2016). Saunders et al. (1997) and Storey et al. (2007) demonstrate that the bulk of volcanism occurred at 62 Ma and at 56 Ma (Figure 11b). Episodic volcanism occurred on east Greenland between 40 and 15 Ma, on west Greenland between 35 and 25 Ma, and on the northwest European Shelf between 45 and 40 Ma. Plate reconstructions show that these patches of volcanism are spread over thousands of kilometers, albeit in regions where earlier volcanism is unequivocally attributed to the growing plume head (Jones & White, 2003; Storey et al., 2007). This pattern of sporadic off-axis volcanism is difficult to explain by a propagating rift hypothesis that is restricted to the spreading axis unless the presence of a convective plume is also invoked.

Since the insight of Vogt (1972), there has been a growing body of indirect evidence for Neogene changes in the bathymetric height of the Greenland-Scotland ridge, which constitutes a significant oceanic gateway (Parnell-Turner et al., 2015; Poore et al., 2006, 2011; Robinson et al., 2011; Wright & Miller, 1996). For example, a global inventory of  $\delta^{13}\text{C}$  measurements from benthic foraminifera combined with the accumulation rate of fine-grained contourite drifts suggests that the amount of deep-water overflow at the Greenland-Scotland ridge varied over the last 7 Ma (Poore et al., 2006; Parnell-Turner et al., 2015). This variation correlates with an entirely independent estimate of changing regional dynamic support based upon V-shaped ridge analysis (Parnell-Turner et al., 2015; Poore et al., 2011). Vertical motions of the Greenland-Scotland ridge are unlikely to have been directly controlled by ridge axial processes per se since the elastic thickness of oceanic lithosphere is  $\leq 30$  km (McKenzie & Bowin, 1976; Watts, 2001). Thus, flexural loading associated with rift propagation along the orthogonal Reykjanes Ridge is very unlikely to influence the Greenland-Scotland ridge, which is ~600 km away.

There is also evidence for transient epeirogeny at distances of up to 1,000 km from the center of the plume during Paleogene times. Along the fringing margins of the North Atlantic Ocean, a series of erosional surfaces were carved into postrift marine strata. In the Faroe-Shetland and North Sea basins, these buried ephemeral landscapes have been mapped on three-dimensional seismic reflection surveys (Shaw Champion et al., 2008; Hartley et al., 2011; Rudge et al., 2008; Smallwood & White, 2002; Stucky de Quay et al., 2017). Subaerial exposure generally lasted less than 0.5 Ma, and landscape unconformities are both underlain and buried by marine sedimentary rocks. Reconstructions of the vertical movements show that up to 1 km of transient uplift grew and decayed within several million years (Hartley et al., 2011).

These rapid, paired, uplift-subsidence events cannot easily be accounted for either by sea level fluctuations or by magmatic underplating. Instead, Rudge et al. (2008) suggested that they more plausibly explained by horizontal advective of thermal anomalies beneath the continental lithosphere. In their kinematic model, radial Poiseuille flow away from the center of the plume is assumed to occur within an asthenospheric channel that is  $150 \pm 50$  km thick. A thermal anomaly of 50–100°C with a flow velocity of up to 40 cm yr<sup>-1</sup> is required to account for the amplitude and duration of transient uplift events mapped in the Faroe-Shetland and North Sea basins. The propagating rift hypothesis cannot account for these Paleogene transient epeirogenic events which occurred at a distance of ~500 km from the putative mid-oceanic ridge system at this time.

#### 4.1.2. Melt Generation and Crustal Thickness at Ridge Axis

Geochemical analysis and modeling of basaltic rocks dredged from the Reykjanes Ridge provides a useful way to test the propagating rift hypothesis. At young propagating rifts, melting is expected to be deeper

and of smaller volume than at established rifts since the younger rift propagates into cooler, thicker lithosphere. Juxtaposition of a young spreading center with cold lithosphere will also cause rapid cooling and tend to produce high degrees of fractionation (e.g., Clague et al., 1981; Hey et al., 1980; Sinton et al., 1983). Consequently, melt generated at the tips of propagating rifts and fracture zones is expected to have distinct major and trace element compositions with anomalously high values of  $\text{FeO}^*/\text{MgO}$ , where  $\text{FeO}^*$  refers to total Fe content, and of  $\text{TiO}_2$  (e.g., Langmuir & Bender, 1984; Sinton et al., 1983).

At the Galapagos spreading center near  $95^\circ\text{W}$  where rift propagation plays a significant role,  $\text{FeO}^*/\text{MgO}$  values of 2–5 and  $\text{TiO}_2$  values of 2.93 wt % are reported for dredged tholeiitic basalts that are <50 km behind the propagating rift tip (Christie and Sinton, 1981, 1986; Sinton et al., 1983).  $\text{FeO}^*/\text{MgO}$  ratios have significantly lower values of  $\sim 1$  along segments of the mid-oceanic ridge away from these propagating rift tips. Thus, the propagating rift hypothesis predicts distinctive major and trace element enrichment in the vicinity of propagating rift tips that correspond to intersections between newly formed pseudofaults and the ridge axis itself (i.e., where a new V-shaped trough with thinner crust is being formed). On Iceland, an example of this process is observed at the southern tip of the southward propagating Eastern Volcanic Zone. Here alkali basalt magmas are generated at Vestmannaeyjar by low degrees of melting that occur beneath thick lithosphere and that are accompanied by enriched trace element compositions (Furman et al., 1991; Meyer et al., 1985; Walters et al., 2013).

Along the Reykjanes Ridge itself, observed offsets of transform faulting are small (2–7 km; Benediktsdóttir et al., 2012). Nonetheless, compositional variations are expected to occur. A combination of geochemical observations of dredged basalts and crustal thickness measurements partly agree with this expectation, since enriched trace element compositions coincide with thinner crust at V-shaped troughs (Jones et al., 2014; Murton et al., 2002; Poore et al., 2011). Along the Reykjanes Ridge, the anticipated variation in major element concentrations (e.g.,  $\text{FeO}^*/\text{MgO}$ ,  $\text{TiO}_2$ ) is absent, despite the significance of these variations at propagating rift tips elsewhere. For example, average  $\text{FeO}^*/\text{MgO}$  values at  $58.5^\circ\text{N}$  and  $60.3^\circ\text{N}$ , where the youngest prominent V-shaped trough and ridge intersect the ridge axis, are  $1.32 \pm 0.07$  and  $1.40 \pm 0.08$ , respectively (Murton et al., 2002). Similarly,  $\text{TiO}_2$  concentrations have nearly constant values of 1 wt % between  $57.5^\circ\text{N}$  and  $61.0^\circ\text{N}$  where V-shaped ridges and troughs are clearly expressed. It is reasonable to conclude that although small-scale propagators along the Reykjanes Ridge may exist, the absence of the expected major element compositional differences casts doubt upon the applicability of the propagating rift hypothesis as a means for explaining the formation of V-shaped ridges and troughs.

An important test for any hypothesis is the requirement to explain why crustal thickness varies by  $\pm 2$  km between V-shaped ridges and troughs (White et al., 1995). At the tip of VSR 1, which is located  $\sim 400$  km away from the center of the plume, the average zero-age crustal thickness is  $10.0 \pm 0.5$  km (Figure 5; Smallwood & White, 1998). Farther south, where the next V-shaped trough intersects the Reykjanes Ridge, the projected average crustal thickness is  $7.8 \pm 0.5$  km, which produces a linear bathymetric depression and a negative free-air gravity anomaly (Figure 5).

Propagating rift models do not explicitly incorporate or predict crustal thickness variations. In applying this model to the Reykjanes Ridge, Hey et al. (2010) draw upon a comparison with crustal thickness measurements at a propagating rift on the Juan Fernandez microplate in the Pacific Ocean. Here a series of profiles across the propagating rift show positive Bouguer gravity anomalies of 5–15 mGal (Kruse et al., 2000). These small positive values could be attributed either to thin or to unusually dense crust, as a consequence of the trade-off between thickness and density. If these gravity anomalies are caused by crustal thickness variations alone, they correspond to a reduction in crustal thickness of 0.3–1 km at the pseudofault itself. Alternatively, these anomalies can be accounted for by an average crustal density excess across the pseudofault of several percent (Kruse et al., 2000). Either way, it is difficult to see how rift propagation alone can produce a crustal thickness difference of over 2 km between the youngest V-shaped ridge and trough pair at the Reykjanes Ridge.

Finally, rift propagation cannot account for a zero-age crustal thickness of 10 km. For a half-spreading rate of 1 cm/yr in the absence of elevated asthenospheric temperature, oceanic crust is expected to have a thickness that is similar to the global mean of  $7.1 \pm 0.8$  km (White et al., 1992). The existence of anomalously thickened crust beneath the Reykjanes Ridge is generally attributed to the presence of a large-scale asthenospheric thermal anomaly associated with the plume (Jones, White, & Maclennan, 2002; Poore et al., 2011; Smallwood & White, 1998; Vogt, 1971). We acknowledge that anomalously thick crust can also be generated by compositional variations within the mantle source which can enhance melting (Foulger & Anderson, 2005). However,

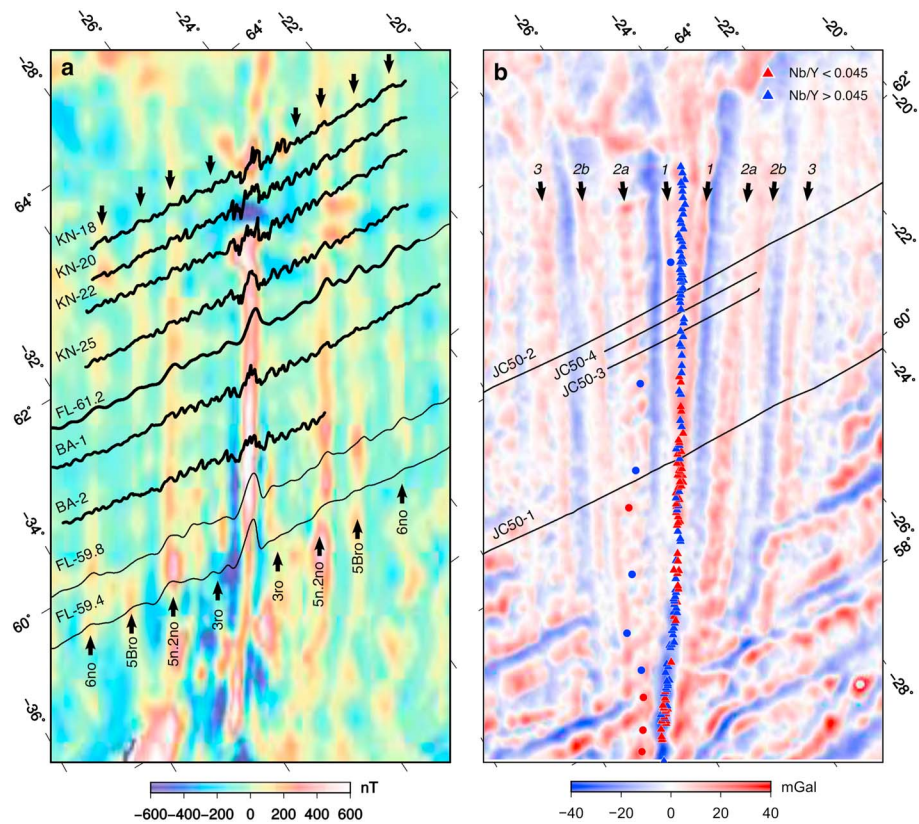


**Figure 13.** (a) Gridded magnetic anomaly map (Maus et al., 2009). Thick lines prefixed by KN and BA = shipboard magnetic anomaly profiles obtained during RV *Knorr* cruise 189-04 and USNS *Bartlett* cruise 75G, respectively (Hey et al., 2010; Nunns et al., 1983); thin lines prefixed by FL = magnetic anomaly profiles extracted from gridded compilation of Maus et al. (2009) along selected flow lines; labeled arrows = identified magnetic chrons. (b) Satellite free-air gravity anomaly map high-pass filtered to remove wavelengths >250 km (Sandwell et al., 2014). Labeled black lines = seismic reflection profiles, colored triangles/circles = locations of basaltic rocks dredged during RRS *Charles Darwin* cruise CD80 and RV *Celtic Explorer* cruise CE0806, respectively, where color indicates Nb/Y value (Jones et al., 2014; Murton et al., 2002), labeled arrows = V-shaped ridges.

the observed combination of crustal thickness and trace element variation can only be adequately matched by invoking asthenospheric temperature changes beneath the ridge axis (Jones et al., 2014; Poore et al., 2011). In this regard, a purely propagating rift hypothesis is a less convincing explanation.

#### 4.1.3. Seafloor Spreading Asymmetry

The propagating rift hypothesis requires that seafloor is accreted asymmetrically either side of the Reykjanes Ridge (Hey et al., 2010). Here we assess the extent of crustal asymmetry between the ridge and a distance of  $\pm 250$  km (i.e., polarity chron 6n at 20.1 Ma) using a set of nine flow line-parallel magnetic anomaly profiles that are spaced every  $\sim 50$  km (Figure 13a). Where available, we exploit shipboard magnetic data from RV *Knorr* cruise 189-04 and from USNS *Bartlett* cruise 75G (Hey et al., 2010; Nunns et al., 1983). Significant gaps are filled using the aeromagnetic compilation of Maus et al. (2009).

Preliminary examination of magnetic anomalies shown in Figure 13a indicates that the principal isochrons (i.e., 5n.2no, 5Bro, and 6no) are broadly symmetrical about the central magnetic anomaly high (CAMH). Figure 14 presents flow line profiles and respective magnetic picks plotted as a function of distance away from the ridge axis. This axis is defined as the center of the CAMH. Following Benediktsdóttir et al. (2012), picks are made at the edges of selected polarity chrons based upon the locus of steepest gradient. Ages are assigned using the timescale of Cande and Kent (1995). Mean half-spreading rates between chron 6n and the present day are calculated by independently applying a linear fit to picks east and west of the axis (Figure 14a). Mean half-spreading rates on the western (i.e., North American) flank are  $11.1 \pm 0.1$  km Ma<sup>-1</sup> and do not vary significantly from north to south. In contrast, spreading rates on the eastern (i.e., Eurasian) flank show some degree of variability. For example, along the northernmost profile, KN-18, the half-spreading rate is 1.1 km Ma<sup>-1</sup>

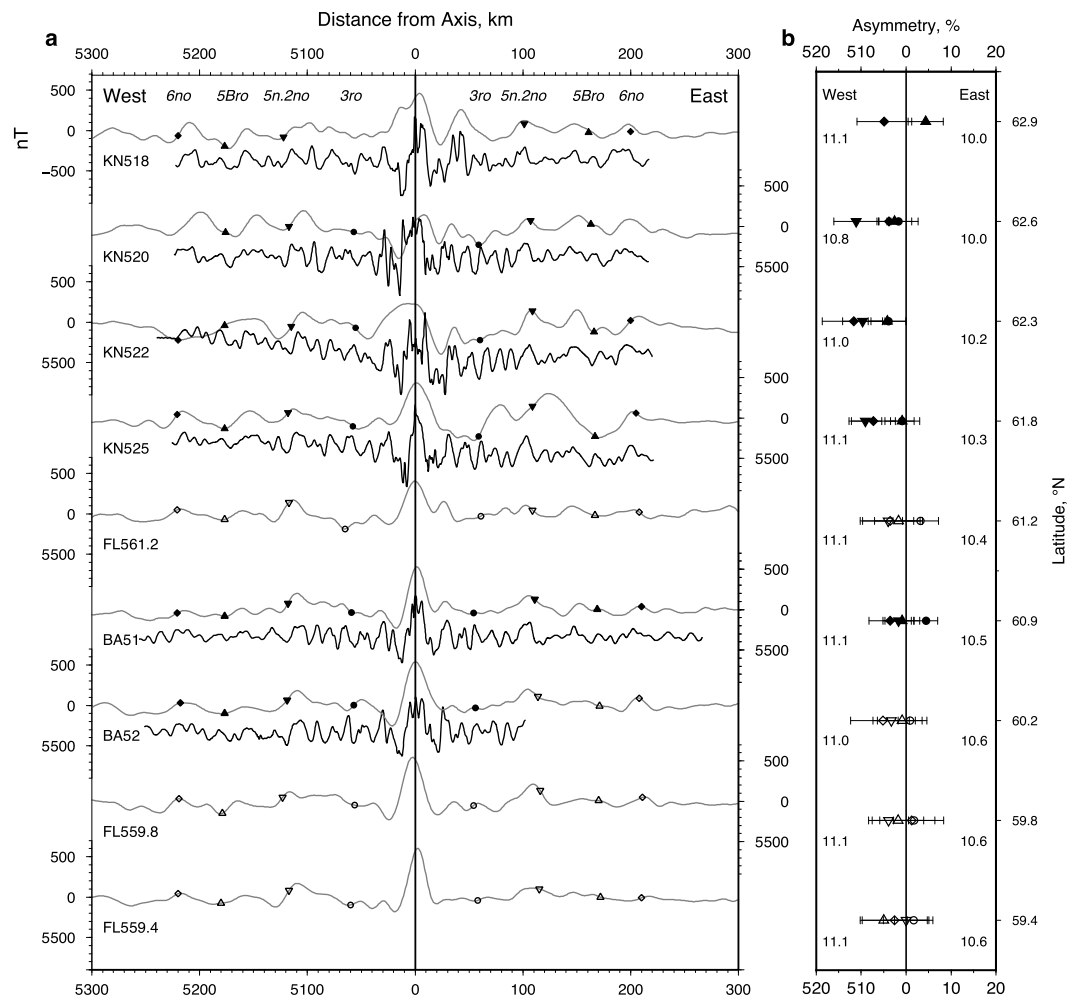


**Figure 14.** (a) Ridge-centered magnetic anomaly profiles (see Figure 13 for location). Black lines prefixed by KN and BA = shipboard magnetic profiles from RV *Knorr* cruise 189-04 and USNS *Bartlett* cruise 75G, respectively (Hey et al., 2010; Nunns et al., 1983), gray lines prefixed by FL = profiles extracted from gridded compilation of Maus et al. (2009) along selected flow lines, filled/open symbols = polarity chrons picked using shipboard/aeromagnetic data, respectively (circles = 3ro, inverted triangles = 5n.2no, triangles = 5Bro, diamonds = 6no). Picks for profiles prefixed by KN are from Benediktsdóttir et al. (2012). (b) Asymmetry as function of latitude, with half-spreading rate west/east in km/Ma noted. Symbols with horizontal lines = asymmetry for time intervals defined by polarity chron picks and associated uncertainties from Benediktsdóttir et al. (2012) and from this study. Positive values of asymmetry indicates extra accretion to east of axis.

slower in the east than in the west (Figure 14b). This difference clearly decreases southward so that it is only  $0.6 \text{ km Ma}^{-1}$  along the southernmost profile, FL-59.4.

The amount of asymmetry within four time intervals defined by polarity chron picks is shown in Figure 14b. Spreading asymmetry can be expressed as a percentage by measuring the distance between successive magnetic anomalies to the east and to the west of the spreading axis. These distances are normalized using the cumulative amount of seafloor generated during that time interval. We start by examining the interval between the present day and chron 3ro (i.e., 0–6.0 Ma; Figure 14b). An additional 5% of crust has been accreted on the eastern side of the axis north of  $62.3^\circ\text{N}$  (compare profiles KN-18, KN-20, and KN-22). This result is consistent with that of Benediktsdóttir et al. (2012) and implies that a modest amount of asymmetric accretion occurred in the region closest to Iceland. South of  $62.3^\circ\text{N}$ , the amount of asymmetry during the same interval is negligible.

The observed asymmetry for intervals of up to 20 Ma reveal a similar pattern. The degree of asymmetry north of  $62.3^\circ\text{N}$  is up to 10% on either side of the axis. South of  $62.3^\circ\text{N}$ , crustal accretion is symmetric within error. If propagating rifts are responsible for generating V-shaped ridges, we would expect to see asymmetric crustal

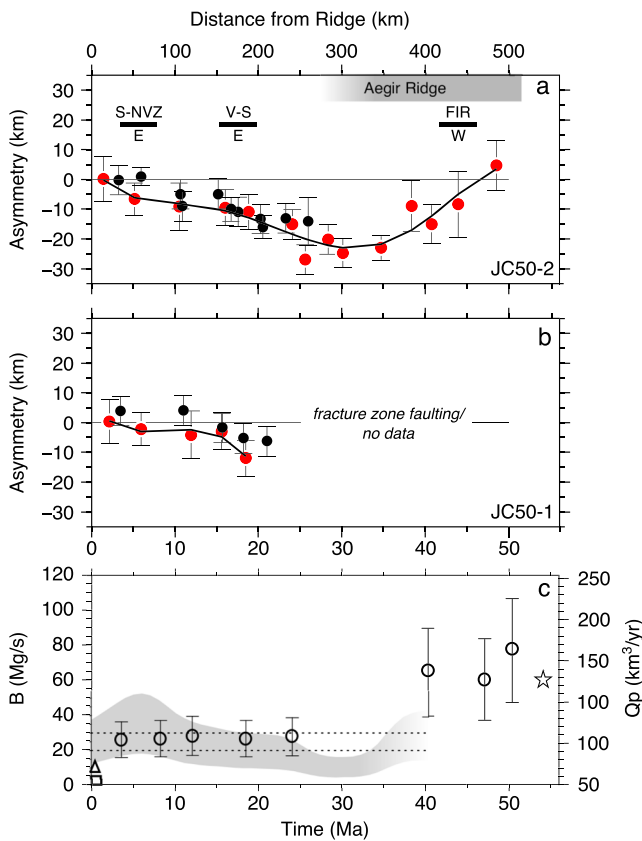


**Figure 15.** Asymmetry along flow line profiles and record of ridge jump episodes from Iceland. (a) Asymmetry along JC50-2 profile where positive values indicate extra accretion to east of Reykjanes Ridge. Black/red circles with error bars = asymmetry values and associated uncertainties calculated from magnetic chron picks and from residual depth profiles, respectively, black curve = best fitting polynomial relationship; labeled horizontal bars = ridge jump episodes recorded on Iceland where E or W indicates compass direction of jump, S-NVZ = Snaefellsnes-Húnaflói paleorift toward Northern Volcanic Zone, V-S = Vestfirðir paleorift toward Snaefellsnes paleorift; FIR = Faroe-Iceland Ridge (Smallwood & White, 2002), gray band = duration of active spreading at Aegir Ridge. (b) Asymmetry along JC50-1 profile. (c) Buoyancy flux,  $B$ , of plume as function of time. Circles with error bars = flux estimates calculated from geometry of V-shaped ridges, square = flux estimate calculated from plume-ridge interaction (Sleep, 1990), star = flux estimate calculated from application of radial Poiseuille flow model (Rudge et al., 2008), gray band = flux estimate calculated from locus of boundary between fractured and smooth oceanic crust (Poore et al., 2009), pair of dotted lines = range of flux estimates obtained from present-day planform of plume swell (Hoggard et al., 2016), triangle = flux estimate for Hawaiian plume (Sleep, 1990).

accretion along the entire ridge axis. Instead, a detectable southward decrease in the amount of asymmetry strongly implies that this process is restricted to a region north of  $\sim 62^\circ\text{N}$  adjacent to Iceland.

It is instructive to compare the pattern of asymmetry determined from magnetic chrons with that of actual V-shaped ridges visible on seismic profiles JC50-1 and 2 (Figure 15). VSR asymmetry is gauged by first identifying conjugate VSR pairs and then measuring their distance from the ridge axis. VSR loci are picked using a combination of residual depth measurements and satellite gravity anomalies. Note that conjugate VSR pairs cannot be reliably identified within the fractured lobes on JC50-1. At distances of less than 250 km from the axis, the amounts of asymmetry determined from magnetic chron picks and VSR morphology are in good agreement. A pattern of increasing asymmetry with distance (i.e., age) from axis is consistent with the well-documented history of ridge jumps on Iceland itself and with the overall history of seafloor spreading within the North Atlantic Ocean (Figure 15a). The most easily recognized ridge jumps on Iceland are those which shift rift axes eastward in order to maintain their positions on top of the center of the plume conduit as the plume itself drifts eastward (Smallwood & White, 2002). The most recent jump occurred between 7 and 3 Ma when rifting shifted from Snaefellsnes-Húnaflói to the Northern Volcanic Zone. A second eastward jump from the Vestfirðir paleorift to the Snaefellsnes paleorift occurred at  $\sim 16$  Ma (Hardarson & Fitton, 1997; Saemundsson, 1974). Both of these events coincide with times when additional crust was accreted along the western side of the Reykjanes Ridge (Figure 15). The opposite trend is seen at  $\sim 40$  Ma, when Smallwood et al. (1999) argued that two westward ridge jumps from the Faroe-Iceland Ridge occurred. This episode coincides with a time interval when additional crust was being accreted along the eastern side of Reykjanes Ridge and when active spreading was taking place at the now-extinct Aegir Ridge (Jung & Vogt, 1997; Smallwood & White, 2002). We suggest that ridge jump activity on Iceland could be responsible for minor, southward declining amounts of asymmetry observed along the Reykjanes Ridge.

#### 4.2. Buoyant Mantle Upwelling

Martinez and Hey (2017) propose a different axial process by which shallow buoyant mantle upwelling instabilities develop along the mid-oceanic ridge and generate the observed crustal structure on either side of the Reykjanes Ridge (see also Murton et al., 2002). In this qualitative model, subaxial cells of buoyant mantle initiate close to Iceland and propagate southward, driven by gradients in subplate properties (e.g., water content, temperature, and composition). Although these cells are said to propagate axially, rapid horizontal flow is not envisaged. Mantle upwelling generates locally increased crustal thickness and accounts for the development of diachronous V-shaped ridges that flank the linear Reykjanes Ridge (Martinez & Hey, 2017). By changing the pattern of mantle advection, removal of segmentation increases melt production and crustal thickness without requiring variations in mantle temperature. This hypothesis aims to avoid the need for three elements of the pulsing plume model: high flow velocities within a horizontal asthenospheric channel,

transient thermal anomalies, and a rheological dehydration boundary which is inferred to deflect plume material in the vicinity of the conduit (e.g., Ito, 2001; Jones, White, & MacLennan, 2002; Poore et al., 2009; Vogt, 1971; White & Lovell, 1997).

This upwelling mechanism invokes a series of buoyant patches of mantle that initiate beneath Iceland where mantle viscosity is lowest and the dry solidus deepest (Martinez & Hey, 2017). These patches are thought to propagate southward beneath the linear Reykjanes Ridge. They are confined between the wet and dry solidi which gradually shallow in the direction of propagation (Martinez & Hey, 2017). The mechanism by which this succession of buoyant patches are generated is not described. Although the patches must propagate

at speeds of  $\sim 40$  cm/yr along the spreading axis, Martinez and Hey (2017) state that “buoyant flow is primarily vertical: it is only the temporal sequence of this flow that propagates horizontally along axis so that rapid horizontal mantle flow is not implied.” Beneath the ridge itself, buoyantly driven flow at a spreading ridge is expected to produce highly depleted melts that are generated by melting of the source region by more than 50% (Spiegelman, 1996). This extreme depletion of highly incompatible elements is inconsistent with geochemical analysis of basaltic rocks dredged from the Reykjanes Ridge (Jones et al., 2014; Murton et al., 2002).

An important shortcoming of buoyant mantle upwelling along the Reykjanes Ridge is that, like rift propagation, this hypothesis fails to account for a range of significant observations that are generally attributed to the spatial and temporal evolution of the plume. The first set of observations is concerned with present-day geophysical and geologic anomalies centered on Iceland. Residual depth measurements demonstrate that oceanic lithosphere throughout the North Atlantic region is 1–2 km shallow than expected. This anomalously shallow footprint is consistent with long-wavelength free-air gravity anomalies that reach from Baffin Bay to western Norway and from Newfoundland to Svalbard. Travel time and full-waveform tomographic models of the North Atlantic region indicate that a 100–200 km thick layer of anomalously slow shear wave velocity lies immediately beneath the lithospheric plates (Delorey et al., 2007; Rickers et al., 2013). Together, these regional observations provide compelling evidence for the presence of a substantial convective upwelling centered on Iceland.

A second set of observations is concerned with Neogene and Paleogene volcanism and regional epeirogeny. Away from the Reykjanes Ridge with which the buoyant mantle upwelling hypothesis is directly concerned, there is evidence for significant off-axis igneous activity, transient dynamic support of oceanic gateways, and regional epeirogeny cannot easily be accounted for by an axially restrictive model whereby patches of buoyant mantle are envisaged as being confined within a narrow corridor that is  $< 100$  km wide (Barnouin-Jha et al., 1997; Bonatti et al., 2003; Scott & Stevenson, 1989). Since oceanic lithosphere has a small elastic thickness, loading effects generated by cells of buoyant upwelling are unlikely to have regional consequences.

### 4.3. Radial Advection of Thermal Anomalies

A thermal pulsing model for the development of V-shaped ridges has become better established since it was originally proposed (Vogt, 1971). This hypothesis has gained acceptance mostly because of its ability to account for a diverse set of Neogene and Paleogene observations. It is also corroborated by fluid dynamical arguments and by convective modeling. In this way, geochemical observations from Iceland and along the Reykjanes Ridge, oceanic crustal thickness measurements, the temporal distribution of regional volcanism, transient epeirogeny, ancient oceanic circulation, and deep-water contourite deposition can be brought together in a single coherent framework.

Nevertheless, some puzzling and unsatisfactory aspects of the thermal pulsing model have given rise to alternative models. Here we scrutinize four of these aspects in turn. Our primary goal is to show that potentially problematic issues can be incorporated within a thermal pulsing framework.

#### 4.3.1. Rheological Dehydration Boundary

Ito (2001) presents a numerical convective model that predicts the generation of diachronous V-shaped ridges from the temporal evolution of radial flow within the head of a plume by imposing time dependency in the form of flux variation within the conduit. A significant feature of this model is the requirement of an increase in viscosity by 2 orders of magnitude close to the base of the primary melt production zone. Numerical simulations show that in the absence of this restriction an unrealistically large amount of melt (i.e., crust) is generated beneath Iceland. The justification is that viscosity is expected to increase when hydrous phases are preferentially extracted from the upward flowing mantle during the earliest stages of decompression partial melting (Hirth & Kohlstedt, 1996). It is important to emphasize that including this rheological dehydration boundary is not a necessary condition for V-shaped ridge formation itself. Instead, it is a possible solution for the problem of excessive melting within a plume head that sits beneath a mid-oceanic ridge (Ito, 2001).

The principal objective of the buoyant mantle upwelling hypothesis is to sidestep this requirement for a dehydration boundary. Martinez and Hey (2017) argue that the existence of this boundary would prevent plume volcanism along the Reykjanes Ridge. Instead, their hypothesis attributes all melting to a plate spreading mechanism. They also infer that the weakness of invoking a rheological boundary is that negligible melting would occur with the head of a mantle plume located in an intraplate setting (e.g., Hawaii).

By combining geochemical modeling of basaltic rocks with crustal thickness measurements on Iceland itself, Maclennan et al. (2001) showed that active upwelling is confined to depths >100 km and that up to 2% melting is expected to occur within this deeper region. Numerical models constrained by geochemical observations suggest that development of the Hawaiian plume is also consistent with small degrees of deep-seated melting (e.g., Putirka, 1999; Putirka et al., 2007; Watson & McKenzie, 1991). Transient convective models of the Iceland plume usually include a component of small degree, deep-seated melting (e.g., Jones et al., 2014; Walters et al., 2013).

Melt generation at the Reykjanes Ridge must be able to account for a combination of crustal thickness and geochemical measurements. We concur with Martinez and Hey (2017) that a low viscosity channel probably exists beneath the mid-oceanic ridge, in agreement with seismic tomographic models. We also acknowledge that buoyant anomalies appear to propagate along the ridge. These observations suggest that melt generation cannot be solely attributed to plate spreading. Regardless of whether these propagating anomalies are thermal or compositional, the requirement for a rheological dehydration boundary beneath the center of the plume is a separate issue.

#### 4.3.2. Asymmetric Crustal Accretion

Hey et al. (2010) and Benediktsdóttir et al. (2012) have used detailed bathymetric and magnetic surveys south of Iceland to show that crustal accretion is not perfectly symmetric on either side of the Reykjanes Ridge. This significant observation accords with evidence for ridge jumps on Iceland itself and with the analysis of crustal accretion along the Greenland-Scotland ridge presented by Smallwood and White (1998). In agreement with Benediktsdóttir et al. (2012), we also find crustal asymmetry of  $\pm 10\%$  north of  $62^\circ\text{N}$  during the last 6 Ma (Figure 14b). This degree of asymmetry is consistent with asymmetric crustal accretion and rift propagation on Iceland, which is evidently affecting that portion of the Reykjanes Ridge north of  $\sim 61.8^\circ\text{N}$ .

Critically, we show that the degree of asymmetry systematically decreases southward so that it is negligible in the region where V-shaped ridges are currently forming at  $60\text{--}61^\circ\text{N}$  (Figure 14b). Here crustal accretion is broadly symmetrical over the last 20 Ma within uncertainty. This observation implies that the effects of rift propagation are either absent or secondary in the region where VSR 1 is actively growing.

Residual depth analysis of regional seismic profiles JC50-1 and JC50-2 demonstrate a similar pattern of asymmetric accretion that is consistent with the Neogene chronology of ridge jumps on Iceland (Parnell-Turner et al., 2014) and with the cessation of seafloor spreading at the now-extinct Aegir Ridge. We conclude that asymmetric crustal accretion is restricted to within 350 km of the plume and that it is probably controlled by rift relocation events that are triggered by changes within the plume itself rather than by rift propagation along the Reykjanes Ridge.

#### 4.3.3. Mantle Source Heterogeneity

The thermal pulsing model implies that the fluctuations in melt volume which give rise to V-shaped ridges are principally, but not exclusively, caused by thermal anomalies within the asthenospheric mantle (Poore et al., 2011). It has been proposed that changes in melt volume, and thus crustal thickness, could be produced by melting of mantle compositional heterogeneities (Murton et al., 2002). These heterogeneities could be long-lived, and it has been suggested that they reflect the presence of ancient oceanic crust subducted during closure of the Iapetus Ocean (Foulger & Anderson, 2005).

The key observations that help to resolve this debate comprise geochemical analyses of basaltic glasses dredged from the Reykjanes Ridge and coincident crustal thickness measurements obtained from wide-angle seismic surveys (Figure 13b; Jones et al., 2014; Murton et al., 2002; Schilling, 1973; Smallwood & White, 1998). A detailed along-axis comparison of bathymetry, gravity anomalies, crustal thickness, and geochemical analyses are shown in Figure 16. These combined observations show that VSRs are clearly associated with trace element compositional variations. Significantly, there is no corresponding variation in Mg number, and so the observed pattern cannot simply be accounted for by fractional crystallization (Jones et al., 2014). Instead, ratios of incompatible trace elements indicative of increased melt fraction (e.g., Nb/Y) inversely correlate with crustal thickness. This inverse relationship is significant because it shows that compositionally enriched basalts are associated with thinner crust (Jones et al., 2014; Murton et al., 2002; Poore et al., 2011). An important corollary is that there is a positive correlation between average melt fraction and crustal thickness, which suggests that temperature fluctuations within the source region moderate crustal thickness. Critically, the opposite correlation is expected when composition is the primary control of melt volume.

Poore et al. (2011) use an inverse modeling approach to show that a  $25^\circ\text{C}$  change in asthenospheric potential temperature,  $T_p$ , is required to simultaneously match the pattern of rare earth element distribution and crustal



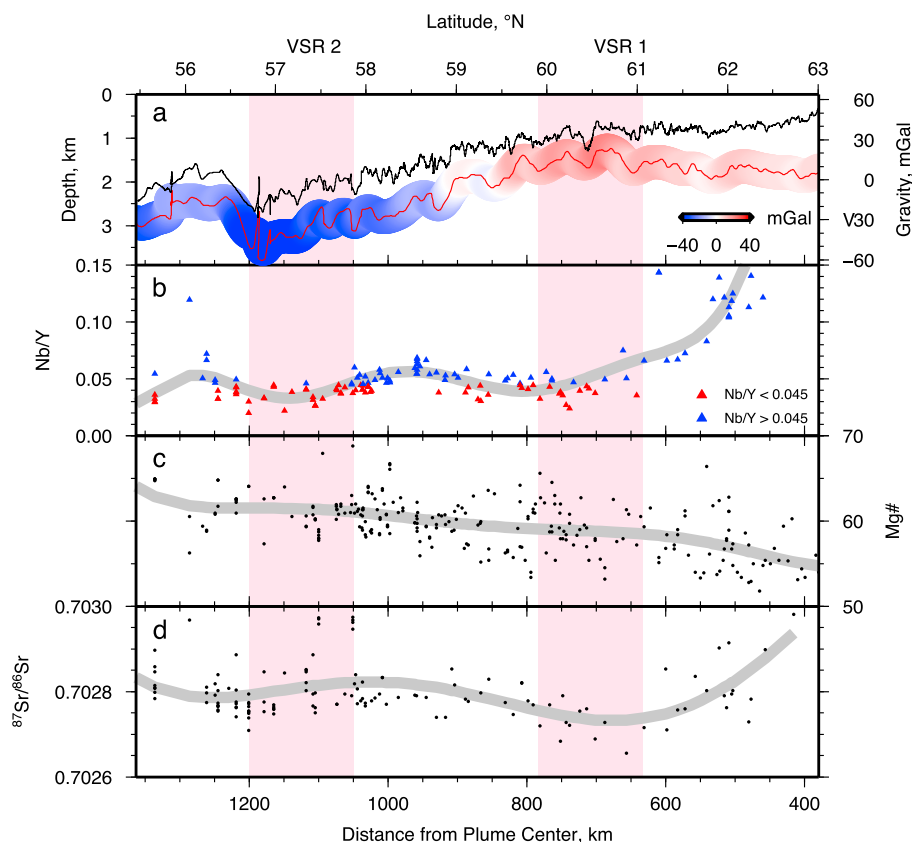


**Figure 16.** Geochemical analyses of basaltic rocks dredged along Reykjanes Ridge between 55° and 63° N (Jones et al., 2014; Murton et al., 2002). (a) Black line = bathymetry as function of latitude, red line with red/blue band = short-wavelength free-air gravity anomaly within 10 km wide corridor as function of latitude. (b) Measured values of trace element ratio Nb/Y as function of latitude. Red/blue triangles = values of Nb/Y as indicated, gray band = best fit polynomial curve. (c) Mg number, Mg#, as function of latitude. (d)  $^{87}\text{Sr}/^{86}\text{Sr}$  measurements as function of latitude. Pair of pink bands delineate regions where V-shaped ridges VSR1 and VSR2 intersect Reykjanes Ridge (Parnell-Turner et al., 2013).

thickness for the youngest pair of V-shaped ridges and troughs. This result agrees with that previously obtained by (White et al., 1995). Jones et al. (2014) used a time-dependent melting model to estimate the peak-to-peak variation of a thermal anomaly as it advects through the melting region. Their results confirm that average values of  $T_p$  calculated using simpler steady state melting models are sufficiently accurate. In this way, a combined geochemical and geophysical analysis of the active ridge axis broadly supports the thermal pulsing model.

#### 4.3.4. Channelized Flow

The thermal pulsing model implies that blobs of anomalously hot mantle material ascend the plume conduit. This transient behavior may reflect interaction between the background mantle flow and flow within a deformable conduit or it may be caused by the growth of instabilities at the thermal boundary layer (Ito, 2001; Olson & Christensen, 1986; Schubert et al., 1989). Alternatively, steady conduit flow could be interrupted by episodic rift relocation on Iceland itself (Hardarson & Fitton, 1997; White et al., 1995). This role for rift location is quite different from that envisaged by Hey et al. (2010), who suggested that rift relocation events propagate along the Reykjanes Ridge to generate V-shaped ridges, independent of any plume-related flow. This channelizing concept is partly supported by seismic anisotropic measurements that imply for restricted, as opposed to radial, flow beneath the spreading axis. It is also possible that flow is moderated by transform offsets (Albers & Christensen, 2001; Gaherty, 2001; Sleep, 2002; Tilmann & Dahm, 2008).

While channelized flow could be adapted to successfully predict geochemical and crustal thickness observations along the Reykjanes Ridge, there is independent evidence for radial flow. First, the distribution of residual depth anomalies in the North Atlantic Ocean is indicative of a roughly circular plume swell that extends over several thousand kilometers (Figure 1a). This distribution is far greater than the putative <100 km wide

melting region which is thought to sit beneath the spreading ridge. A thin (100–200 km) layer of anomalously slow shear wave velocity coincides with the plume swell (Rickers et al., 2013). These geophysical observations are consistent with inverse modeling of trace element compositions and crustal thickness observations within central Iceland which indicate that significant plume-driven flow occurs only at depths >100 km (MacLennan et al., 2001). Finally, distal observations of off-axis volcanism, long period fluctuations of ancient deep-water circulation driven by transient epeirogeny of oceanic gateways, and the existence of buried ephemeral landscapes along fringing continental margins are difficult to explain by channelized flow beneath the ridge axis alone (e.g., Shaw Champion et al., 2008; Poore et al., 2006; Wilkinson et al., 2016).

#### 4.4. Implications of Transient Plume Activity

Our evaluation of different hypotheses that attempt to explain formation of V-shaped ridges suggests that the thermal pulsing model satisfactorily accounts for a range of geophysical, geochemical, and geologic observations within the oceanic basins and along the fringing continental margins. Here we discuss the wider implications of this model for the geometry for crustal accretion and for the fluid dynamics of convective plumes.

The notion of transient thermal anomalies is neither new nor unexpected. The Rayleigh number of the upper mantle is supercritical by 3 to 5 orders of magnitude, which means that it is expected to exhibit time-dependent behavior (Schubert et al., 2001). This existence of time-dependent convective circulation is predicted by theoretical analysis, by laboratory experiments, and by numerical simulations. It is generally acknowledged that blobs of variable viscosity can be advected around convection cells, which suggests that transient activity may be a general phenomenon (e.g., Ito, 2001; Olson & Christensen, 1986; Ribe et al., 2007; Schubert et al., 1989). There is little evidence that the subaxial cells of buoyant upwelling, invoked by Martinez and Hey (2017) to explain plume pulsing in the absence of thermal anomalies, occur within other plumes. For example, variations in melt production along the Hawaii-Emperor Seamount Chain have been interpreted to represent pulsing of the Hawaiian plume every ~5 Ma (Ark Van & Lin, 2004; Vidal & Bonneville, 2004). An obvious difficulty is that Hawaii is located far from any spreading axes, and so axial buoyant mantle upwelling is an improbable mechanism. If the buoyant mantle upwelling hypothesis is only applicable to ridge-centered plumes, it is still necessary to explain why other plumes exhibit transient activity.

The regional seismic reflection profiles presented here allow us to identify changes in crustal accretion under constant spreading rate conditions. It is evident that changes in crustal architecture are affected by changes in the balance between magmatic and tectonic processes. Our observations suggest that two distinct modes of plate spreading along the Reykjanes Ridge exist; the first mode produces relatively smooth crust, free of fracture zones; the second mode that produces crust associated fracture zone faulting.

In the smooth mode, plate spreading is predominantly accommodated by magmatism and V-shaped ridges are observed. This mode of crustal accretion dominates along a section of the Reykjanes Ridge today, extending 200–950 km away from the center of the plume (Figure 10a). A Paleogene record of this smooth mode can be seen on oceanic crust >40 Ma in age, where brittle extension is minimal and where buried V-shaped ridges are visible.

The rugose mode of plate spreading produces crust dominated by fracture zones with an apparent lack of VSRs. Jones, White, Clarke, et al. (2002) suggest that an apparent absence of VSRs within the fractured lobes may not necessarily imply a lack of asthenospheric temperature fluctuations. Although the dominance of fracture zones within these lobes makes it difficult to identify VSRs, the great reduction in the size of the plume during this period suggests that VSRs are absent given that a significant reduction in the magmatic fraction of plate separation along portions of JC50-1 on both sides of the spreading axis closely matches the region of fracturing identified from satellite gravity data.

A changing ratio of faulting and magmatism is most easily interpreted as a consequence of mantle potential temperature which varies when the planform of the plume grows or decays. Minor ( $\pm 25^\circ\text{C}$ ) variations in potential temperature at the ridge axis causes kilometer-scale changes in the depth to the brittle-plastic transition which in turn alters the balance between the amount of magmatic accretion and normal faulting (Parnell-Turner et al., 2013). We propose that the style of crustal accretion is highly sensitive to subtle changes in potential temperature so that the two modes of accretion faithfully record spatial waxing and waning of this plume through Cenozoic times.

**Table 1**

*Buoyancy Flux, B, Mass Flux, M, Volume Flux, V, Propagation Velocity, c, and Time of Origin, t, for Inferred Thermal Anomalies Obtained by Fitting Radial Model to Geometries of Observed V-Shaped Ridges (see Figure 10b for Locations of Labeled V-Shaped Ridges)*

VSR	<i>B</i> (Mg s <sup>-1</sup> )	<i>M</i> (kg yr <sup>-1</sup> × 10 <sup>14</sup> )	<i>V</i> (km <sup>3</sup> yr <sup>-1</sup> )	<i>c</i> (km Ma <sup>-1</sup> )	<i>t</i> (Ma)
1	26.2 ± 10.2	1.9 ± 0.3	57.5 ± 1.1	150.5 ± 18.5	3.6 ± 0.4
2a	26.8 ± 10.4	1.9 ± 0.4	58.6 ± 1.1	132.5 ± 22.5	8.3 ± 0.2
2b	28.4 ± 11.1	2.0 ± 0.4	62.3 ± 1.2	148.0 ± 30.0	12.1 ± 0.1
3	26.8 ± 10.4	1.9 ± 0.3	58.6 ± 1.1	130.0 ± 5.0	18.5 ± 1.2
4	27.9 ± 10.8	2.0 ± 0.4	61.1 ± 1.2	162.5 ± 13.5	24.0 ± 0.3
5	64.4 ± 25.1	4.5 ± 0.9	141.2 ± 2.8	400.0 ± 40.0	40.3 ± 0.3
6	60.2 ± 23.4	4.2 ± 0.8	132.1 ± 2.6	242.0 ± 4.0	47.1 ± 0.4
7	76.8 ± 29.8	5.4 ± 1.1	168.3 ± 3.4	567.0 ± 4.0	50.4 ± 0.4

*Note.* Errors propagated by assuming asthenospheric layer,  $h = 125 \pm 25$  km, and temperature anomaly,  $\Delta T = 150 \pm 50^\circ$ .

#### 4.5. Plume Flux Estimates

The buoyancy flux of the Iceland plume can be inferred from the geometry of the V-shaped ridges (Jones et al., 2014; Poore et al., 2009; Vogt, 1971; White & Lovell, 1997). Before acquisition of the regional seismic reflection profiles described here, it was only possible to use the bathymetric and gravitational expression of Neogene VSRs to calculate buoyancy flux (Poore et al., 2009). More complete residual depth profiles described here allow us to identify the existence and geometry of Paleogene VSRs with confidence which means that the record of buoyancy flux can be extended back to ~50 Ma. If plume material flows radially away from Iceland, buoyancy flux,  $B$ , is given by

$$B = \left( \frac{\pi h \rho_m \alpha \Delta T}{t} \right) r^2 \quad (2)$$

where  $h$  is thickness of the plume layer,  $\rho_m$  is the density of mantle,  $\alpha$  is the thermal expansion coefficient,  $\Delta T$  is the temperature difference between the plume and ambient mantle, and  $t$  is the time taken for a VSR to travel from the center of the plume out to a radial distance,  $r$  (see Table B1). For each VSR, loci in age-distance space were picked based upon residual depth profiles and gravity anomalies (Figure 10). Equation (2) is used to fit these loci (Figure 10b).

The Cenozoic variation of buoyancy flux with time is shown in Figure 15 and listed in Table 1. Note that time is taken to be the moment at which a given thermal anomaly was at zero distance from the center of the plume. For VSRs that are younger than 24 Ma (i.e., 1, 2a, 2b, 3, and 4), we obtain a buoyancy flux of  $25 \pm 5$  Mg s<sup>-1</sup>. Steeper gradients of older VSRs (i.e., 5, 6, and 7) yield higher buoyancy fluxes ranging from 60 to 77 Mg s<sup>-1</sup>. These values compare well with independent estimates. Using sparse bathymetric and magnetic data from the youngest VSRs alone, Vogt (1971) estimated the volume flux to be 10–100 km<sup>3</sup> yr<sup>-1</sup>, equivalent to a buoyancy flux of 7–70 Mg s<sup>-1</sup>. The changing boundary between smooth and fractured oceanic crust yields buoyancy fluxes of 10–50 Mg s<sup>-1</sup> for the last 35 Ma (Poore et al., 2009; Figure 15c).

The present-day planform of the Iceland plume swell can be determined from residual depth measurements and used to constrain its excess volume (Crosby & McKenzie, 2009; Hoggard et al., 2016). If the present-day swell grew over the last 23–35 Ma, the average buoyancy flux is 20–30 Mg s<sup>-1</sup> (Figure 15c). Analysis of buried Paleogene landscapes on the northwest European shelf implies that the plume originally had a much higher buoyancy flux of 60–70 Mg s<sup>-1</sup> (Figure 15c; Rudge et al., 2008).

We acknowledge that these flux estimates are much greater than that calculated by Sleep (1990), who argues that the present-day buoyancy flux of the plume is 1.4 Mg s<sup>-1</sup>. This discrepancy arises due to Sleep's assumption that plume material advects away from Iceland at a velocity,  $V$ , that is equal to the plate spreading velocity. Our estimates of  $V$  range from 150 to 162 mm yr<sup>-1</sup> for the past 24 Ma (Table 1). We can recalculate buoyancy flux using Sleep's method with revised values of  $V$  while retaining his original assumptions. In this case, the velocity of the lithospheric plate is  $V_l$  and the asthenospheric velocity is  $V_a$ . Thus asthenospheric material flows

at a velocity  $V_a$  within a channel where velocity decreases linearly from  $V_a$  at the top to zero at the bottom (i.e., Couette flow). The volume flux,  $Q_p$ , is given by

$$Q_p = (V_l t_l + V_a(t_a/2))Y \quad (3)$$

where  $t_l$  is lithospheric thickness,  $t_a$  is the asthenospheric channel thickness away from the ridge, and  $Y$  is the along-strike distance influenced by the plume (Sleep, 1990). Using  $V_l = V_a = 16.5 \text{ mm yr}^{-1}$ ,  $t_l = t_a = 100 \text{ km}$ , and  $Y = 800 \text{ km}$ , Sleep (1990) finds that  $Q_p = 63 \text{ m}^3 \text{ s}^{-1}$ . Assuming  $\Delta T = 225^\circ\text{C}$ , we obtain a buoyancy flux of  $1.4 \text{ Mg s}^{-1}$ , in expected agreement with Sleep (1990). However, if we assume  $V_a = 150 \text{ mm yr}^{-1}$ , using the mean velocity estimated for the youngest V-shaped ridge which is more consistent with Poiseuille flow,  $t_a = 125 \text{ km}$  (Delorey et al., 2007; Rickers et al., 2013), and  $Y = 1,350 \text{ km}$  from geochemical observations (Jones et al., 2014), we obtain  $B = 10.4 \text{ Mg s}^{-1}$ . This value is one order of magnitude greater than that of Sleep (1990) although it is still less than that estimated using equation (2). This discrepancy reflects the assumed decrease of  $V_a$  within the asthenospheric channel. If an average uniform velocity is used within this channel, we obtain  $B = 19.3 \text{ Mg s}^{-1}$ , which is in closer agreement with our estimates.

## 5. Conclusions

Regional seismic reflection profiles, oriented parallel to plate spreading flow lines, have been used to analyze the crustal architecture of the Reykjanes Ridge and the flanking oceanic basins. These profiles reveal a series of basement highs and lows that reach from the Reykjanes Ridge to the continental margins. The variation of the sediment-basement interface correlates with V-shaped ridges and troughs on oceanic crust  $>20 \text{ Ma}$ , which have long been recognized from bathymetric and gravity anomaly profiles. Our findings extend and refine these earlier studies, suggesting that the process of V-shaped ridge formation has been taking place since Eocene times.

We identify changes in the mode of plate spreading at the ridge axis, recorded by variations in the cumulative amount of horizontal extension accommodated by normal faulting. The proportion of magmatic crustal accretion diminished at 33 Ma and increased again at 25 Ma at distances of  $\sim 600 \text{ km}$  away from the plume. This changing proportion coincides with the spatial distribution of fractured, rugose oceanic crust on either side of the Reykjanes Ridge. These patterns imply subtle changes in mantle potential temperature that are probably caused by changes in the planform of the plume. We suggest that oceanic crustal architecture is highly sensitive to the spatial distribution of hot, subplate asthenospheric material.

The chronology of the North Atlantic Igneous Province shows that widespread, episodic volcanism occurred over a substantial region between west Greenland and the British Isles throughout Paleogene times. Discrete episodes of volcanism appear to coincide with V-shaped ridge activity and with evidence for transient epeirogeny on the northwest European shelf. Equally, the 3–6 Ma periodicity is broadly consistent with the frequency of VSR activity. Evidence for episodic and discontinuous volcanism long after continental breakup suggests that transient pulsing behavior has continued to the present day.

Competing hypotheses that attempt to account for the formation of VSRs have been evaluated using a diverse range of geologic, geophysical and geochemical observations. In light of this evaluation, we assert that the thermal pulsing model remains the most reasonable explanation that is consistent with crustal thickness measurements, geochemical analyses of dredged basaltic rocks, asymmetric crustal accretion, regional dynamic support, off-axis volcanism, changes in ancient deep-water circulation, and distal transient epeirogeny. The rift propagation hypothesis is predicated upon identification of asymmetric ridge accretion identified on high resolution magnetic surveys. We agree that this asymmetry exists but it is minor, and rapidly diminishes southward, which implies that it is related to well-documented ridge jumps on Iceland. The buoyant mantle upwelling hypothesis is invoked to sidestep the need for an upwelling plume with a rheological dehydration boundary beneath Iceland. This hypothesis cannot account for regional observations that strongly support the existence of a convective swell beneath the North Atlantic Ocean. Finally, we have revised buoyancy flux estimates using V-shaped ridge geometry. The flux of the Iceland plume is  $25 \pm 5 \text{ Mg s}^{-1}$  during Neogene times. There is evidence that buoyancy flux was as great  $60\text{--}76 \text{ Mg s}^{-1}$  during Paleogene times.

## Appendix A: Crustal Thickness Estimates

Seabed and top basement horizons were converted from two-way travel time to depth using a two-layer velocity model, with a velocity of  $1.5 \text{ km s}^{-1}$  in the water layer. A sedimentary layer with velocity of  $2.5 \text{ km s}^{-1}$

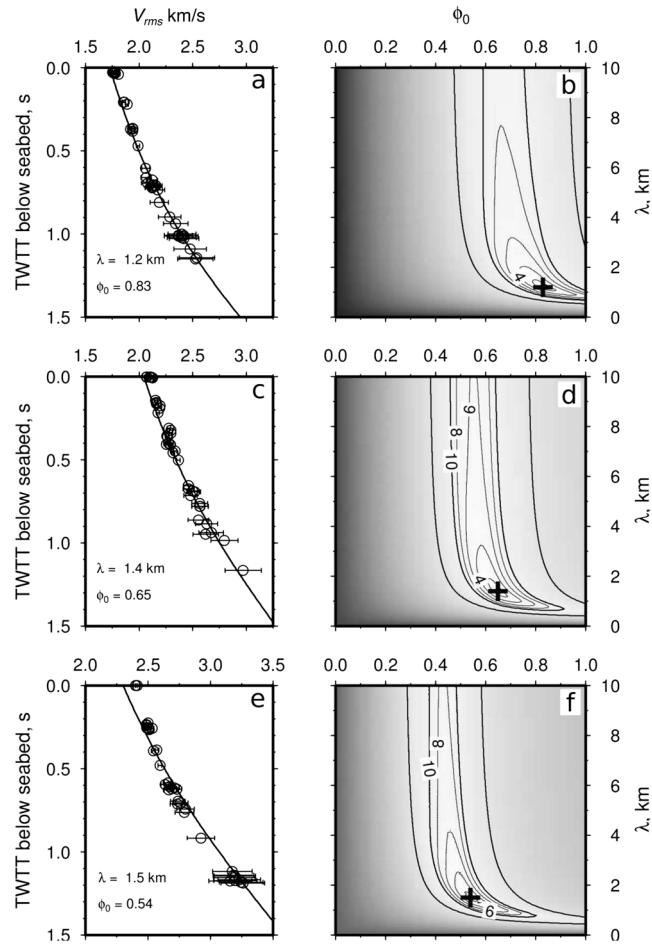


**Figure A1.** Inverse modeling of compaction parameters,  $\phi_0$  and  $\lambda$ , at locations shown in Figure 4. (a) The rms velocity plotted as function of two-way travel time at range of 835 km along profile JC50-2. Circles with error bars = observed rms velocity measurements, solid line = best fit relationship obtained by varying  $\phi_0$  and  $\lambda$ . (b) Root-mean-square misfit plotted as function of  $\phi_0$  and  $\lambda$  (equation (A6)). Black cross = location of global minimum. (c and d) Analysis at range of 65 km along profile JC50-1. (e and f) Analysis at range of 930 km along profile JC50-1.

was used, which is the mean interval velocity from hand-picked stacking velocities along JC50-1 and JC50-2. In order to calculate the water-loaded subsidence of oceanic crust, we first account for the effects of sedimentary loading. An Airy isostatic correction is used to calculate the water-loaded subsidence,  $s_w$ , given by

$$s_w = t_w + \left( \frac{\rho_a - \bar{\rho}_s}{\rho_a - \rho_w} \right) t_s \quad (\text{A1})$$

where  $t_w$  and  $t_s$  are water depth and sediment thickness, respectively (Le Douaran, 1982). Density of asthenosphere is  $\rho_a = 3.3 \text{ g cm}^{-3}$  and density of seawater is  $\rho_w = 1.0 \text{ g cm}^{-3}$ . Average density of a sedimentary pile,  $\bar{\rho}_s$ , is approximated by

$$\bar{\rho}_s = (1 - \bar{\phi})\rho_s + \bar{\phi}\rho_w \quad (\text{A2})$$

where  $\rho_s = 2,700 \text{ kg m}^{-3}$  is the density of sediment grains and  $\bar{\phi}$  is the average porosity, which depends upon the thickness of the sedimentary pile.  $\bar{\phi}$  is given by

$$\bar{\phi} = \frac{1}{t_s} \int_0^{t_s} \phi_0 \exp(-z/\lambda_s) dz = \frac{\phi_0 \lambda_s}{t_s} (1 - \exp(-t_s/\lambda_s)) \quad (\text{A3})$$

where  $\phi_0$  is initial porosity,  $\lambda_s$  is compaction decay length, and  $z$  is depth. Compaction parameters,  $\phi_0$  and  $\lambda_s$ , were obtained by inversion of stacking velocities for individual CMPs (Walford & White, 2005). In a region

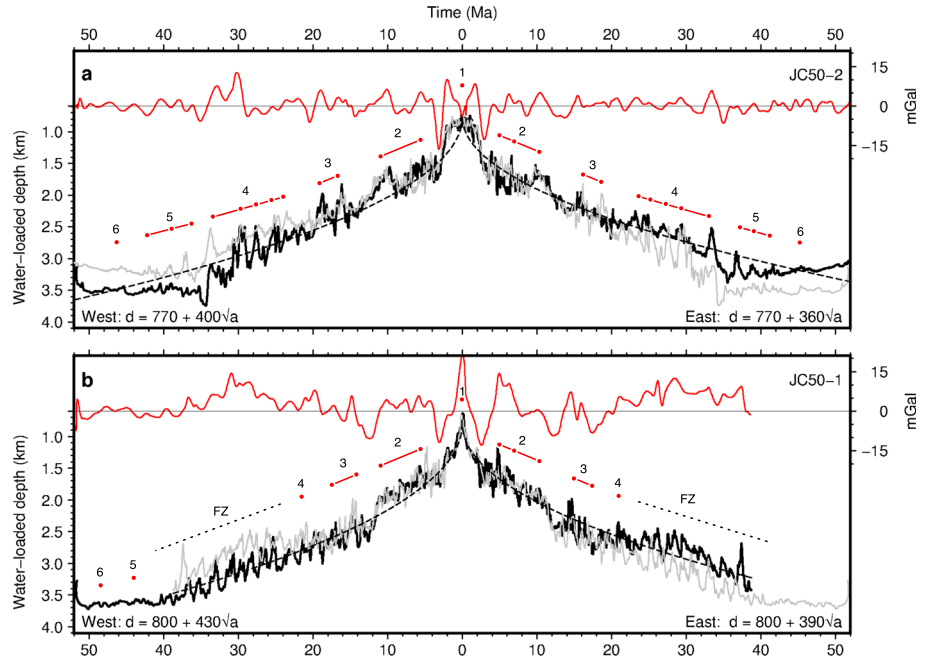


**Figure A2.** Bathymetric analyses. (a) Profile JC50-2. Solid line = water-loaded depth to basement as function of seafloor age calculated from seismic reflection profile shown in Figure 4a, gray line = water-loaded depth to basement mirrored about spreading axis, dashed line = best fit age-depth relationship that describes subsidence of oceanic crust (coefficients of best fitting model given for eastern/western portions of profile), numbered red dotted-dashed lines = identifiable V-shaped ridges, red line = free-air gravity anomaly (Sandwell et al., 2014). (b) Profile JC50-1. Black dotted lines labeled FZ = regions where fracture zone faulting predominates.

of uniform lithology, the primary control on seismic interval velocity is likely to be the porosity of the medium, which is itself controlled by compaction. Interval velocity,  $V_{int}$ , is given by

$$\frac{1}{V_{int}} = \frac{\phi}{V_{fl}} + \frac{(1-\phi)}{V_{ma}} \quad (A4)$$

where  $V_{fl}$  and  $V_{ma}$  are velocities of the pore fluid =  $1.5 \text{ km s}^{-1}$  and rock matrix (assumed to be dominated by the  $P$  wave velocity of quartz) =  $6.0 \text{ km s}^{-1}$  (Christensen, 1982; Wyllie et al., 1956). Combining equation (A3) with equation (A4), we obtain  $V_{int}(z)$ . Estimates of root-mean-square (rms) velocity,  $V_{rms}$ , are generated when performing routine velocity analysis as part of the seismic processing sequence.  $V_{rms}$  can be described as a function of two-way travel time,  $t$ , where

$$V_{rms}^2 = \frac{\int_0^t V_{int}(t)^2 dt}{t} \quad (A5)$$

The inversion procedure seeks a combination of  $\phi_0$  and  $\lambda_s$  which minimizes the misfit function,  $M(\phi_0, \lambda_s)$ , between the modeled  $V_{rms}$  profile,  $V^c$ , and the observed  $V_{rms}$  profile,  $V^o$ , as a function of two-way travel time. A least squares method is used to minimize the residual misfit function  $M$ , which is defined as

$$M = \sqrt{\frac{1}{n} \sum_{i=1}^n \left( \frac{V_i^o - V_i^c}{\sigma_i} \right)^2} \quad (A6)$$

where  $n$  is the number of data points and  $\sigma_i$  is the error in observed  $V_{rms}$ . The right hand side of equation (A6) is a least squares fit between  $V^c$  and  $V^o$ . Velocity profiles were picked every 100 CMPs (~625 m spacing) based upon semblance analyses and constant velocity stack panels. The half-width of a semblance peak was used to estimate error on measured velocities at 150 equally spaced CMP locations along JC50-2. From  $t < 520 \text{ ms}$ , the error is  $15 \text{ m s}^{-1}$ . For  $t > 520 \text{ ms}$ , the average error is estimated using a least squares fit to the picked semblance half-widths as a function of  $t$ , expressed as

$$\sigma_i = 0.234t - 109 \text{ m s}^{-1} \quad (A7)$$

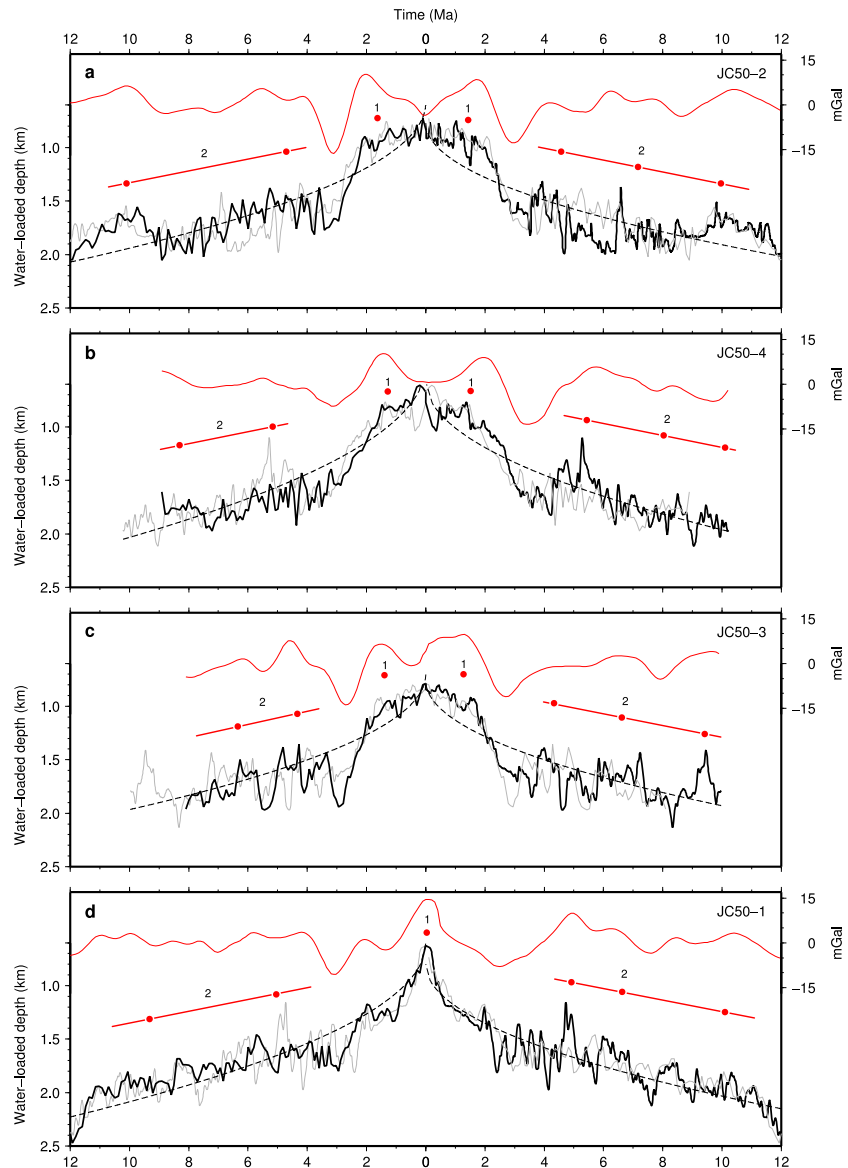


**Figure A3.** Detailed bathymetric analyses of VSRs 1 and 2. (a) Profile JC50-2. Solid line = water-loaded depth to basement as function of seafloor age calculated from seismic reflection profile shown in Figure 4a, gray line = water-loaded depth to basement mirrored about spreading axis, dashed line = best fit age-depth relationship that describes subsidence of oceanic crust, numbered red dotted-dashed lines = identifiable V-shaped ridges, red line = free-air gravity anomaly (Sandwell et al., 2014). (b) Profile JC50-4. (c) Profile JC50-3. (d) Profile JC50-1.

Inversion results for three CMPs are shown in Figure A1. Inverse modeling was carried out at 1,000 CMP intervals, and typically yields  $\phi_0 = 0.5-0.85$  and  $\lambda_s = 1-2$  km. These values are consistent with measurements from North Atlantic sedimentary cores, which yield  $\phi_0 = 0.6$  and  $\lambda_s = 2$  km (Le Douaran, 1982). With knowledge of water depth, sediment thickness and compaction parameters, water-loaded depth to basement is calculated using equation (A1). Water-loaded depth to basement profiles are shown in Figures A2 and A3.

Oceanic ages were assigned using magnetic anomaly picks from a compilation of shipboard and aeromagnetic surveys (Jones, White, & Maclennan, 2002; Maus et al., 2009). The difference between observed water-loaded depth and predicted age-depth relationship for thermal subsidence of an oceanic plate is the residual depth,  $d_r$ . Since the oceanic crust is less than 60 Ma in age, plate subsidence can be simply expressed as

$$d = d_r + c\sqrt{a} \tag{A8}$$

**Table B1**  
Variables and Constants Used in Buoyancy Flux Calculations

Symbol	Description	Value	Unit
$\Delta T$	Excess plume temperature (Poore et al., 2009; White, 1997)	$150 \pm 50$	$^{\circ}\text{C}$
$h$	Vertical thickness of plume head (Deloey et al., 2007)	$125 \pm 25$	km
$\rho_m$	Density of lithospheric mantle	$3.2 \times 10^3$	$\text{kg m}^{-3}$
$\alpha$	Thermal expansion coefficient (Chopelas & Boehler, 1992)	$3 \times 10^{-5}$	$^{\circ}\text{C}^{-1}$

where  $d$  is the water-loaded subsidence of oceanic crust,  $d_i$  is the depth of the mid-oceanic ridge at zero age,  $a$  is the age of oceanic crust, and  $c$  is a constant controlling the rate of lithospheric cooling. Observed water-loaded depth to basement profiles can be fitted to the predicted plate subsidence using a least squares method, producing best fitting values for  $d_i$  and  $c$  (Figures A2 and A3). The fitting procedure is carried out separately for eastern and western portions of each profile to allow for variations in dynamic support. Crustal thickness,  $t_c$ , can be estimated from

$$t_c \approx \left( \frac{\rho_a - \rho_w}{\rho_a - \rho_c} \right) d_r + t_{\text{ref}} \quad (\text{A9})$$

where  $\rho_a = 3.3 \text{ g cm}^{-3}$  is the density of asthenosphere,  $\rho_c = 2.8 \text{ g cm}^{-3}$  is the density of crust, and  $t_{\text{ref}} = 8.4 \text{ km}$  is a reference crustal thickness for this region (Smallwood & White, 1998).

## Appendix B: Buoyancy Flux Calculation Parameters

Table B1 summarizes the principle variables and constants that are used for buoyancy calculations. We acknowledge that the quoted values have important uncertainties, but these uncertainties do not materially affect our conclusions regarding the buoyancy flux of the Iceland plume.

### Acknowledgments

This research project was supported by Natural Environment Research Council grant NE/G007632/1, by the Girdler Fund, University of Cambridge, and by BP Exploration. We thank A. Crosby, I. Frame, M. Hoggard, D. Lyness, and J. Winterbourne for their help. We thank Á. Benediktsdóttir, an anonymous Reviewer, and the Associate Editor for helpful comments. We pay tribute to the Master, crew, and scientific party of RRS *James Cook* Cruise JC50 for their dedication and professionalism. Seismic reflection survey is available upon request from NJW (njw10@cam.ac.uk). University of Cambridge Earth Sciences contribution number esc.4045.

### References

- Albers, M., & Christensen, U. R. (2001). Channeling of plume flow beneath mid-ocean ridges. *Earth and Planetary Science Letters*, *187*, 207–220.
- Allen, R. M., Nolet, G., Morgan, W. J., Vogfjörð, K., Nettles, M., Ekström, G., ... Stefaönsson, R. (2002). Imaging the mantle beneath Iceland using integrated seismological techniques. *Journal of Geophysical Research*, *107*(B12), 2325. <https://doi.org/10.1029/2001JB000595>
- Ark Van, E., & Lin, J. (2004). Time variation in igneous volume flux of the Hawaii-Emperor hot spot seamount chain. *Journal of Geophysical Research*, *109*, B11401. <https://doi.org/10.1029/2003JB002949>
- Barnouin-Jha, K., Parmentier, E. M., & Sparks, D. W. (1997). Buoyant mantle upwelling and crustal production at oceanic spreading centers: On-axis segmentation and off-axis melting. *Journal of Geophysical Research*, *102*(B6), 11,979–11,989. <https://doi.org/10.1029/96JB03807>
- Behn, M., & Ito, G. (2008). Magmatic and tectonic extension at mid-ocean ridges: 1. Controls on fault characteristics. *Geochemistry, Geophysics, Geosystems*, *9*, Q08O10. <https://doi.org/10.1029/2008GC001965>
- Benediktsdóttir, Á., Hey, R., Martínez, F., & Hoskuldsson, A. (2012). Detailed tectonic evolution of the Reykjanes Ridge during the past 15 Ma. *Geochemistry, Geophysics, Geosystems*, *13*, Q02008. <https://doi.org/10.1029/2011GC003948>
- Bianchi, G. G., & McCave, I. N. (2000). Hydrography and sedimentation under the deep western boundary current on Björn and Gardar Drifts, Iceland Basin. *Marine Geology*, *165*(1), 137–169.
- Bonatti, E., Ligi, M., Brunelli, D., Cipriani, A., Fabretti, P., Ferrante, V., ... Ottolini, L. (2003). Mantle thermal pulses below the Mid-Atlantic Ridge and temporal variations in the formation of oceanic lithosphere. *Nature*, *423*, 499–505. <https://doi.org/10.1038/nature01594>
- Brevik, A. J., Mjelde, R., Faleide, J. I., & Murai, Y. (2006). Rates of continental breakup magmatism and seafloor spreading in the Norway Basin–Iceland plume interaction. *Journal of Geophysical Research*, *111*, B07102. <https://doi.org/10.1029/2005JB004004>
- Briais, A., & Rabinowicz, M. (2002). Temporal variations of the segmentation of slow to intermediate spreading mid-ocean ridges. 1. Synoptic observations based on satellite altimetry data. *Journal of Geophysical Research*, *107*(B5), ECV 3–1–ECV 3–17. <https://doi.org/10.1029/2001JB000533>
- Buck, W. R., Lavier, L., & Poliakov, A. N. B. (2005). Modes of faulting at mid-ocean ridges. *Nature*, *434*, 719–723. <https://doi.org/10.1038/nature03358>
- Cande, S. C., & Kent, D. V. (1995). Revised calibration of the geomagnetic polarity timescale for the Late Cretaceous and Cenozoic. *Journal of Geophysical Research*, *100*(B4), 6093–6095.
- Chopelas, A., & Boehler, R. (1992). Thermal expansivity in the lower mantle. *Geophysical Research Letters*, *19*, 1983–1986.
- Christensen, N. I. (1982). Seismic velocities. In R. S. Carmichael (Ed.), *Handbook of physical properties of rocks* (Vol. 2, pp. 47–74). Boca Raton, FL: CRC Press.
- Christie, D. M., & Sinton, J. M. (1981). Evolution of abyssal lavas along propagating segments of the Galapagos spreading center. *Earth and Planetary Science Letters*, *56*, 321–335. [https://doi.org/10.1016/0012-821X\(81\)90137-0](https://doi.org/10.1016/0012-821X(81)90137-0)
- Christie, D. M., & Sinton, J. M. (1986). Major element constraints on melting, differentiation and mixing of magmas from the Galapagos 95.5°W propagating rift system. *Contributions to Mineralogy and Petrology*, *94*(3), 274–288. <https://doi.org/10.1007/BF00371437>
- Clague, D. A., Frey, F., Thompson, G., & Rindge, S. (1981). Minor and trace element geochemistry of volcanic rocks dredged from the Galapagos spreading center: Role of crystal fractionation and mantle heterogeneity. *Journal of Geophysical Research*, *86*, 9469–9482. <https://doi.org/10.1029/JB086iB10p09469>



- Crosby, A. G., & McKenzie, D. P. (2009). An analysis of young ocean depth, gravity and global residual topography. *Geophysical Journal International*, 178(3), 1198–1219. <https://doi.org/10.1111/j.1365-246X.2009.04224.x>
- Davis, M. W., White, N. J., Priestley, K. F., Baptie, B. J., & Tilmann, F. J. (2012). Crustal structure of the British Isles and its epeirogenic consequences. *Geophysical Journal International*, 190, 705–725. <https://doi.org/10.1111/j.1365-246X.2012.05485.x>
- Delorey, A., Dunn, R. A., & Gaherty, J. B. (2007). Surface wave tomography of the upper mantle beneath the Reykjanes Ridge with implications for ridge-hot spot interaction. *Journal of Geophysical Research*, 112, B08313. <https://doi.org/10.1029/2006JB004785>
- Engdahl, E. R., van der Hilst, R., & Buland, R. (1998). Global teleseismic earthquake relocation with improved travel times and procedures for depth determination. *Bulletin of the Seismological Society of America*, 88(3), 722–743.
- Faithfull, J. W., Timmerman, M. J., Upton, B. G. J., & Rumsey, M. S. (2012). Mid-Eocene renewal of magmatism in NW Scotland: The Loch Roag Dyke, Outer Hebrides. *Journal of the Geological Society*, 169, 115–118. <https://doi.org/10.1144/0016-76492011-117>
- Foulger, G. R., & Anderson, D. L. (2005). A cool model for the Iceland hotspot. *Journal of Volcanology and Geothermal Research*, 141, 1–22. <https://doi.org/10.1016/j.jvolgeores.2004.10.007>
- Furman, T., Frey, F. A., & Park, K. H. (1991). Chemical constraints on the petrogenesis of mildly alkaline lavas from Vestmannaeyjar, Iceland: The Eldfell (1973) and Surtsey (1963–1967) eruptions. *Contributions to Mineralogy and Petrology*, 109, 19–37. <https://doi.org/10.1007/BF00687198>
- Gaherty, J. B. (2001). Seismic evidence for hotspot-induced buoyant flow beneath the Reykjanes Ridge. *Science*, 293, 1645–1647.
- Ganerød, M., Smethurst, M. A., Torsvik, T. H., Prestvik, T., Rouse, S., van Hinsbergen, D. J. J., & Hendriks, B. W. H. (2010). The North Atlantic Igneous Province reconstructed and its relation to the Plume Generation Zone: The Antrim Lava Group revisited. *Geophysical Journal International*, 182, 183–202. <https://doi.org/10.1111/j.1365-246X.2010.04620.x>
- Geikie, A. (1889). The history of volcanic action during the tertiary period in the British Isles. *Transactions of the Royal Society of Edinburgh: Earth Sciences*, 35, 21–184.
- Hardarson, B., & Fitton, J. G. (1997). Mechanisms of crustal accretion in Iceland. *Geology*, 25, 1043–1046.
- Hartley, R. A., Roberts, G. G., White, N. J., & Richardson, C. (2011). Transient convective uplift of an ancient buried landscape. *Nature Geoscience*, 4, 562–565.
- Hey, R., Duenebier, F. K., & Morgan, W. J. (1980). Propagating rifts on midocean ridges. *Journal of Geophysical Research*, 85(B7), 3647–3658. <https://doi.org/10.1029/JB085iB07p03647>
- Hey, R., Martinez, F., Höskuldsson, Á., & Benediktssdóttir, Á. (2010). Propagating rift model for the V-shaped ridges south of Iceland. *Geochemistry, Geophysics, Geosystems*, 11(3), Q03011. <https://doi.org/10.1029/2009GC002865>
- Hey, R., Martinez, F., Höskuldsson, Á., Eason, D. E., Sleeper, J., Thordarson, S., ... Merkuriev, S. (2016). Multibeam investigation of the active North Atlantic plate boundary reorganization tip. *Earth and Planetary Science Letters*, 435, 115–123. <https://doi.org/10.1016/j.epsl.2015.12.019>
- Hirth, G., & Kohlstedt, D. L. (1996). Water in the oceanic upper mantle: Implications for rheology, melt extraction and the evolution of the lithosphere. *Earth and Planetary Science Letters*, 144, 93–108.
- Hoggard, M. J., White, N. J., & Al-Attar, D. (2016). Global dynamic topography observations reveal limited influence of large-scale mantle flow. *Nature Geoscience*, 9, 456–463. <https://doi.org/10.1038/ngeo2709>
- Hooff, E. E. E., Brandsdóttir, B., Mjelde, R., & Shimamura, H. (2006). Asymmetric plume-ridge interaction around Iceland: The Kolbeinsey Ridge Iceland Seismic Experiment. *Geochemistry, Geophysics, Geosystems*, 7, Q05015. <https://doi.org/10.1029/2005GC001123>
- Ito, G. (2001). Reykjanes 'V'-shaped ridges originating from a pulsing and dehydrating mantle plume. *Nature*, 411, 681–684. <https://doi.org/10.1038/35079561>
- Johnson, G. L., & Schneider, E. (1969). Depositional ridges in the North Atlantic. *Earth and Planetary Science Letters*, 6, 416–422.
- Jones, S. M. (2003). Test of a ridge-plume interaction model using oceanic crustal structure around Iceland. *Earth and Planetary Science Letters*, 208, 205–218. [https://doi.org/10.1016/S0012-821X\(03\)00050-5](https://doi.org/10.1016/S0012-821X(03)00050-5)
- Jones, S. M., & White, N. J. (2003). Shape and size of the starting Iceland plume swell. *Earth and Planetary Science Letters*, 216(3), 271–282. [https://doi.org/10.1016/S0012-821X\(03\)00507-7](https://doi.org/10.1016/S0012-821X(03)00507-7)
- Jones, S. M., White, N. J., & MacLennan, J. (2002). V-shaped ridges around Iceland: Implications for spatial and temporal patterns of mantle convection. *Geochemistry, Geophysics, Geosystems*, 3(10), 1–23. <https://doi.org/10.1029/2002GC000361>
- Jones, S. M., White, N. J., Clarke, B. J., Rowley, E., & Gallagher, K. (2002). Present and past influence of the Iceland Plume on sedimentation. In A. G. Dore et al. (Eds.), *Exhumation of the North Atlantic margin: Timing, mechanisms and implications for petroleum exploration* (Vol. 196, pp. 13–25). London: Geological Society, London, Special Publications.
- Jones, S. M., Murton, B. J., Fitton, J. G., White, N. J., MacLennan, J., & Walters, R. L. (2014). A joint geochemical-geophysical record of time-dependent mantle convection south of Iceland. *Earth and Planetary Science Letters*, 386, 86–97. <https://doi.org/10.1016/j.epsl.2013.09.029>
- Jung, W.-Y., & Vogt, P. R. (1997). A gravity and magnetic anomaly study of the extinct Aegir Ridge, Norwegian Sea. *Journal of Geophysical Research*, 102(B3), 5065–5089.
- Kruse, S. E., Tebbens, S. F., Naar, D. F., Lou, Q. Y., & Bird, R. T. (2000). Comparisons of gravity anomalies at pseudofaults, fracture zones, and nontransform discontinuities from fast to slow spreading areas. *Journal of Geophysical Research*, 105(B12), 28,399–28,410. <https://doi.org/10.1029/2000JB900281>
- Langmuir, C. H., & Bender, J. F. (1984). The geochemistry of oceanic basalts in the vicinity of transform faults: Observations and implications. *Earth and Planetary Science Letters*, 69(1), 107–127. [https://doi.org/10.1016/0012-821X\(84\)90077-3](https://doi.org/10.1016/0012-821X(84)90077-3)
- Larsen, L. M., Pedersen, A. K., Pedersen, G. K., & Piasecki, S. (1992). Timing and duration of Early Tertiary volcanism in the North Atlantic: New evidence from West Greenland. *Geological Society London Special Publication*, 68, 321–333. <https://doi.org/10.1144/GSL.SP.1992.068.01.20>
- Larsen, L. M., Pedersen, A. K., Tegner, C., & Duncan, R. A. (2014). Eocene to Miocene igneous activity in NE Greenland: Northward younging of magmatism along the East Greenland margin. *Journal of the Geological Society*, 171, 539–553. <https://doi.org/10.1144/jgs2013-118>
- Larsen, L. M., Pedersen, A. K., Sørensen, E. V., Watt, W. S., & Duncan, R. A. (2013). Stratigraphy and age of the Eocene Igtertivå Formation basalts, alkaline pebbles and sediments of the Kap Dalton Group in the graben at Kap Dalton, East Greenland. *Bulletin of the Geological Society of Denmark*, 61, 1–18.
- Larsen, L. M., Heaman, L. M., Creaser, R. A., Duncan, R. A., Frei, R., & Hutchinson, M. (2009). Tectonomagmatic events during stretching and basin formation in the Labrador Sea and the Davis Strait: Evidence from age and composition of Mesozoic to Palaeogene dyke swarms in West Greenland. *Journal of the Geological Society*, 166, 999–1012. <https://doi.org/10.1144/0016-76492009-038>
- Larsen, L. M., Pedersen, A. K., Tegner, C., Duncan, R. A., Hald, N., & Larsen, J. G. (2016). Age of Tertiary volcanic rocks on the West Greenland continental margin: Volcanic evolution and event correlation to other parts of the North Atlantic Igneous Province. *Geological Magazine*, 153(3), 487–511. <https://doi.org/10.1017/S0016756815000515>

- Le Douaran, S. (1982). A note on the correction of ocean floor depths for sediment loading. *Journal of Geophysical Research*, 87(B6), 4715–4722. [https://doi.org/10.1016/0198-0254\(82\)90130-3](https://doi.org/10.1016/0198-0254(82)90130-3)
- Macdonald, K. C., Fox, P. J., Perram, L. J., Eisen, M. F., Haymon, R. M., Miller, S. P., ... Shor, A. N. (1988). A new view of the mid-ocean ridge from the behaviour of ridge-axis discontinuities. *Nature*, 335(6187), 217–225. <https://doi.org/10.1038/335217a0>
- Maclennan, J., McKenzie, D. P., & Gronvold, K. (2001). Plume-driven upwelling under central Iceland. *Earth and Planetary Science Letters*, 194(1–2), 67–82. [https://doi.org/10.1016/S0012-821X\(01\)00553-2](https://doi.org/10.1016/S0012-821X(01)00553-2)
- Martinez, F., & Hey, R. (2017). Propagating buoyant mantle upwelling on the Reykjanes Ridge. *Earth and Planetary Science Letters*, 457, 10–22. <https://doi.org/10.1016/j.epsl.2016.09.057>
- Maus, S., Barckhausen, U., Berkenbosch, H., Bournas, N., Brozena, J., Childers, V., ... Tontini, F. C. (2009). EMAG2: A 2-arc min resolution Earth Magnetic Anomaly Grid. *Geochemistry, Geophysics, Geosystems*, 10, Q08005. <https://doi.org/10.1029/2009GC002471>
- McKenzie, D. P., & Bickle, M. J. (1988). The volume and composition of melt generated by extension of the lithosphere. *Journal of Petrology*, 29, 625–679.
- McKenzie, D. P., & Bowin, C. (1976). The relationship between bathymetry and gravity in the Atlantic Ocean. *Journal of Geophysical Research*, 81(11), 1903–1915. <https://doi.org/10.1029/JB081i011p01903>
- Meyer, P. S., Sigurdsson, H., & Schilling, J.-G. (1985). Petrological and geochemical variations along Iceland's Neovolcanic Zones. *Journal of Geophysical Research*, 90(B12), 10,043–10,072. <https://doi.org/10.1029/JB090iB12p10043>
- Morgan, W. J. (1971). Convection plumes in the lower mantle. *Nature*, 230, 42–43.
- Murton, B. J., Taylor, R. N., & Thirlwall, M. F. (2002). Plume-ridge interaction: A geochemical perspective from the Reykjanes Ridge. *Journal of Petrology*, 43(11), 1987–2012. <https://doi.org/10.1093/petrology/43.11.1987>
- Navin, D. A., Peirce, C., & Sinha, M. C. (1998). The RAMESSES experiment—II. Evidence for accumulated melt beneath a slow spreading ridge from wide-angle refraction and multichannel reflection seismic profiles. *Geophysical Journal International*, 135(3), 746–772. <https://doi.org/10.1046/j.1365-246X.1998.00709.x>
- Nevle, R. J., Brandriss, M. E., Bird, D. K., McWilliams, M. O., & Neil, J. R. O. (1994). Tertiary plutons monitor climate change in East Greenland. *Geology*, 22, 775–778. [https://doi.org/10.1130/0091-7613\(1994\)022<0775](https://doi.org/10.1130/0091-7613(1994)022<0775)
- Nunns, A. G., Talwani, M., Lorentzen, G. R., Vogt, P. R., Sigurdsson, T., Kristjansson, L., ... Voppell, D. (1983). *Magnetic anomalies over Iceland and surrounding seas*. In M. H. P. Bott et al. (Eds.), *Structure and development of the Greenland-Scotland ridge* (pp. 661–678). New York: Plenum Press.
- O'Connor, J. M., Stoffers, P., Wijbrans, J. R., Shannon, P. M., & Morrissey, T. (2000). Evidence from episodic seamount volcanism for pulsing of the Iceland plume in the past 70 Myr. *Nature*, 408, 954–959.
- Olson, P., & Christensen, U. (1986). Solitary wave propagation in a fluid conduit within a viscous matrix. *Journal of Geophysical Research*, 91(B6), 6367–6374.
- Parkin, C. J., & White, R. S. (2008). Influence of the Iceland mantle plume on oceanic crust generation in the North Atlantic. *Geophysical Journal International*, 173, 168–188. <https://doi.org/10.1111/j.1365-246X.2007.03689.x>
- Parnell-Turner, R., White, N. J., Maclennan, J., Henstock, T. J., Murton, B. J., & Jones, S. M. (2013). Crustal manifestations of a hot transient pulse at 60°N beneath the Mid-Atlantic Ridge. *Earth and Planetary Science Letters*, 363, 109–120. <https://doi.org/10.1016/j.epsl.2012.12.030>
- Parnell-Turner, R., White, N. J., Henstock, T., Murton, B. J., Maclennan, J., & Jones, S. M. (2014). A continuous 55-million-year record of transient mantle plume activity beneath Iceland. *Nature Geoscience*, 7, 914–919. <https://doi.org/10.1038/NGEO2281>
- Parnell-Turner, R., White, N. J., McCave, I. N., Henstock, T., Murton, B. J., & Jones, S. M. (2015). Architecture of North Atlantic contourite drifts modified by transient circulation of the Icelandic mantle plume. *Geochemistry, Geophysics, Geosystems*, 16, 3414–3435. <https://doi.org/10.1002/2015GC005947>
- Parsons, B., & Sclater, J. G. (1977). An analysis of the variation of ocean floor bathymetry and heat flow with age. *Journal of Geophysical Research*, 82(5), 803–827.
- Poore, H. R., White, N. J., & Jones, S. M. (2009). A Neogene chronology of Iceland plume activity from V-shaped ridges. *Earth and Planetary Science Letters*, 283, 1–13. <https://doi.org/10.1016/j.epsl.2009.02.028>
- Poore, H. R., White, N. J., & Maclennan, J. (2011). Ocean circulation and mantle melting controlled by radial flow of hot pulses in the Iceland plume. *Nature Geoscience*, 4, 1–4. <https://doi.org/10.1038/ngeo1161>
- Poore, H. R., Samworth, R., White, N. J., Jones, S. M., & McCave, I. N. (2006). Neogene overflow of northern component water at the Greenland-Scotland Ridge. *Geochemistry, Geophysics, Geosystems*, 7, Q06010. <https://doi.org/10.1029/2005GC001085>
- Putirka, K. (1999). Melting depths and mantle heterogeneity beneath Hawaii and the East Pacific Rise: Constraints from Na/Ti and rare earth element ratios. *Journal of Geophysical Research*, 104(B2), 2817–2829. <https://doi.org/10.1029/1998JB900048>
- Putirka, K. D., Perfit, M., Ryerson, F. J., & Jackson, M. G. (2007). Ambient and excess mantle temperatures, olivine thermometry, and active vs. passive upwelling. *Chemical Geology*, 241, 177–206. <https://doi.org/10.1016/j.chemgeo.2007.01.014>
- Ribe, N. M., Davaille, A., & Christensen, U. (2007). Fluid dynamics of mantle plumes. In *Mantle plumes* (pp. 1–48). Berlin: Springer.
- Rickers, F., Fichtner, A., & Trampert, J. (2013). The Iceland–Jan Mayen plume system and its impact on mantle dynamics in the North Atlantic region: Evidence from full-waveform inversion. *Earth and Planetary Science Letters*, 367, 39–51. <https://doi.org/10.1016/j.epsl.2013.02.022>
- Robinson, M. M., Valdes, P. J., Haywood, A. M., Dowsett, H. J., Hill, D. J., & Jones, S. M. (2011). Bathymetric controls on Pliocene North Atlantic and Arctic sea surface temperature and deepwater production. *Palaeogeography, Palaeoclimatology, Palaeoecology*, 309, 92–97. <https://doi.org/10.1016/j.palaeo.2011.01.004>
- Roest, W. R., & Srivastava, S. P. (1989). Geology Sea-floor spreading in the Labrador Sea: A new reconstruction. *Geology*, 17, 1000–1003.
- Rudge, J. F., Shaw Champion, M. E., White, N. J., McKenzie, D. P., & Lovell, B. (2008). A plume model of transient diachronous uplift at the Earth's surface. *Earth and Planetary Science Letters*, 267, 146–160. <https://doi.org/10.1016/j.epsl.2007.11.040>
- Saemundsson, K. (1974). Evolution of the axial rifting zone in Northern Iceland and the Tjörnes Fracture Zone. *Geological Society of America Bulletin*, 85, 495–504. [https://doi.org/10.1130/0016-7606\(1974\)85<495:EOTARZ>2.0.CO;2](https://doi.org/10.1130/0016-7606(1974)85<495:EOTARZ>2.0.CO;2)
- Sandwell, D. T., Muller, R. D., Smith, W. H. F., Garcia, E., & Francis, R. (2014). New global marine gravity model from CryoSat-2 and Jason-1 reveals buried tectonic structure. *Science*, 346, 65–67. <https://doi.org/10.1126/science.1258213>
- Saunders, A. D., Fitton, J. G., Kerr, A. C., Norry, M. J., & Kent, R. W. (1997). The North Atlantic igneous province. In J. J. Mahoney & M. F. Coffin (Eds.), *Large igneous provinces: Continental, oceanic, and planetary flood volcanism* (pp. 45–93). Washington, DC: American Geophysical Union.
- Schilling, J. (1973). Iceland mantle plume: Geochemical study of Reykjanes Ridge. *Nature*, 242, 565–571. <https://doi.org/10.1038/242565a0>
- Schoonman, C., White, N., & Pritchard, D. (2017). Radial viscous fingering of hot asthenosphere within the Icelandic plume beneath the North Atlantic Ocean. *Earth and Planetary Science Letters*, 468, 51–61. <https://doi.org/10.1016/j.epsl.2017.03.036>
- Schubert, G., Olson, P., Anderson, C., & Goldman, P. (1989). Solitary waves in mantle plumes. *Journal of Geophysical Research*, 94(B7), 9523–9532.

- Schubert, G., Turcotte, D. L., & Olson, P. (2001). *Mantle convection in the Earth and planets*. Cambridge, UK: Cambridge University Press.
- Scott, D. R., & Stevenson, D. J. (1989). A self-consistent model of melting, magma migration and buoyancy-driven circulation beneath mid-ocean ridges. *Journal of Geophysical Research*, *94*(88), 2973–2988. <https://doi.org/10.1029/JB094iB03p02973>
- Searle, R. C., Keeton, J., Owens, R., White, R. S., Mecklenburgh, R., Parsons, B., & Lee, S.-M. (1998). The Reykjanes Ridge: Structure and tectonics of a hot-spot-influenced, slow-spreading ridge, from multibeam bathymetry, gravity and magnetic investigations. *Earth and Planetary Science Letters*, *160*, 463–478. [https://doi.org/10.1016/S0012-821X\(98\)00104-6](https://doi.org/10.1016/S0012-821X(98)00104-6)
- Seton, M., Müller, R. D., Zahirovic, S., Gaina, C., Torsvik, T., Shephard, G., ... Chandler, M. (2012). Global continental and ocean basin reconstructions since 200 Ma. *Earth-Science Reviews*, *113*(3-4), 212–270. <https://doi.org/10.1016/j.earscirev.2012.03.002>
- Shaw Champion, M. E., White, N. J., Jones, S. M., & Lovell, J. P. B. (2008). Quantifying transient mantle convective uplift: An example from the Faroe-Shetland basin. *Tectonics*, *27*, 1–18. <https://doi.org/10.1029/2007TC002106>
- Shorttle, O., MacLennan, J., & Jones, S. M. (2010). Control of the symmetry of plume-ridge interaction by spreading ridge geometry. *Geochemistry, Geophysics, Geosystems*, *11*, Q0AC05. <https://doi.org/10.1029/2009GC002986>
- Sinton, J. M., Wilson, D. S., Christie, D. M., & Hey, R. (1983). Petrologic consequences of rift propagation on oceanic spreading ridges. *Earth and Planetary Science Letters*, *62*, 193–207.
- Sleep, N. H. (1990). Hotspots and Mantle Plumes: Some Phenomenology. *Journal of Geophysical Research*, *95*, 6715–6736.
- Sleep, N. H. (2002). Local lithospheric relief associated with fracture zones and ponded plume material. *Geochemistry, Geophysics, Geosystems*, *3*(12), 8506. <https://doi.org/10.1029/2002GC000376>
- Smallwood, J. R., & White, R. S. (1998). Crustal accretion at the Reykjanes Ridge. *Journal of Geophysical Research*, *103*(B3), 5185–5201.
- Smallwood, J. R., & White, R. S. (2002). Ridge-plume interaction in the North Atlantic and its influence on continental breakup and seafloor spreading. *Geological Society London Special Publication*, *197*, 15–37. <https://doi.org/10.1144/GSL.SP.2002.197.01.02>
- Smallwood, J. R., Staples, R. K., Richardson, K. R., & White, R. S. (1999). Crust generated above the Iceland mantle plume: From continental rift to oceanic spreading center. *Journal of Geophysical Research*, *104*(B10), 22,822–22,902.
- Spiegelman, M. (1996). The sensitivity of trace elements to mantle dynamics. *Earth and Planetary Science Letters*, *139*, 115–132.
- Stolt, R. H. (1978). Migration by Fourier transform. *Geophysics*, *43*, 23–48.
- Storey, M., Duncan, R. A., Pedersen, A. K., Larsen, L. M., & Larsen, H. C. (1998). Ar/Ar geochronology of the West Greenland Tertiary volcanic province. *Earth and Planetary Science Letters*, *160*, 569–586.
- Storey, M., Pedersen, A. K., Stecher, O., Bernstein, S., Larsen, H. C., Larsen, L. M., & Baker, J. A. (2004). Long-lived postbreakup magmatism along the East Greenland margin: Evidence for shallow-mantle metasomatism by the Iceland plume. *Geology*, *32*, 173–176. <https://doi.org/10.1130/G19889.1>
- Storey, M., Duncan, R. A., & Tegner, C. (2007). Timing and duration of volcanism in the North Atlantic Igneous Province: Implications for geodynamics and links to the Iceland hotspot. *Chemical Geology*, *241*, 264–281. <https://doi.org/10.1016/j.chemgeo.2007.01.016>
- Stucky de Quay, G., Roberts, G. G., Watson, J. S., & Jackson, C. A.-L. (2017). Incipient mantle plume evolution: Constraints from ancient landscapes buried beneath the North Sea. *Geochemistry, Geophysics, Geosystems*, *18*, 973–993. <https://doi.org/10.1002/2016GC006769>
- Tegner, C., Duncan, R. A., Bernstein, S., Brooks, C. K., Bird, D. K., & Storey, M. (1998). Ar-Ar geochronology of Tertiary mafic intrusions along the East Greenland rifted margin: Relation to flood basalts and the Iceland hotspot track. *Earth and Planetary Science Letters*, *156*, 75–88.
- Tegner, C., Brooks, C., Duncan, R., Heister, L., & Bernstein, S. (2008). <sup>40</sup>Ar/<sup>39</sup>Ar ages of intrusions in East Greenland: Rift-to-drift transition over the Iceland hotspot. *Lithos*, *101*, 480–500. <https://doi.org/10.1016/j.lithos.2007.09.001>
- Tilmann, F. J., & Dahm, T. (2008). Constraints on crustal and mantle structure of the oceanic plate south of Iceland from ocean bottom recorded Rayleigh waves. *Tectonophysics*, *447*, 66–79. <https://doi.org/10.1016/j.tecto.2006.02.028>
- Vidal, V., & Bonneville, A. (2004). Variations of the Hawaiian hot spot activity revealed by variations in the magma production rate. *Journal of Geophysical Research*, *109*, B03104. <https://doi.org/10.1029/2003JB002559>
- Vogt, P. R. (1971). Asthenosphere motion recorded by the ocean floor south of Iceland. *Earth and Planetary Science Letters*, *13*, 153–160.
- Vogt, P. R. (1972). The Faeroe-Iceland-Greenland aseismic ridge and the western boundary undercurrent. *Nature*, *239*, 79–81.
- Vogt, P. R., & Avery, O. E. (1974). Detailed magnetic surveys in the northeast Atlantic and Labrador Sea. *Journal of Geophysical Research*, *79*(2), 363–389.
- Walford, H. L., & White, N. J. (2005). Constraining uplift and denudation of west African continental margin by inversion of stacking velocity data. *Journal of Geophysical Research*, *110*, B04403. <https://doi.org/10.1029/2003JB002893>
- Walters, R. L., Jones, S. M., & MacLennan, J. (2013). Renewed melting at the abandoned Húnaflói Rift, northern Iceland, caused by plume pulsing. *Earth and Planetary Science Letters*, *1*, 1–12. <https://doi.org/10.1016/j.epsl.2013.06.040>
- Watson, S., & McKenzie, D. P. (1991). Melt generation by plumes: A study of Hawaiian volcanism. *Journal of Petrology*, *32*(3), 501–537.
- Watts, A. B. (2001). *Isostasy and flexure of the lithosphere*. Cambridge, UK: Cambridge University Press.
- White, N. J., & Lovell, B. (1997). Measuring the pulse of a plume with the sedimentary record. *Nature*, *387*, 888–891.
- White, R. S. (1997). Rift-plume interaction in the North Atlantic. *Philosophical Transactions of the Royal Society of London: Series A*, *355*, 319–339. <https://doi.org/10.1098/rsta.1997.0011>
- White, R. S., & McKenzie, D. P. (1989). Magmatism at Rift Zones: The generation of volcanic continental margins and flood basalts. *Journal of Geophysical Research*, *94*(B6), 7685–7729. <https://doi.org/10.1029/JB094iB06p07685>
- White, R. S., Bown, J., & Smallwood, J. R. (1995). The temperature of the Iceland plume and origin of outward-propagating V-shaped ridges. *Journal of the Geological Society*, *152*, 1039–1045.
- White, R. S., McKenzie, D. P., & O'Nions, R. K. (1992). Oceanic crustal thickness from seismic measurements and rare earth element inversions. *Journal of Geophysical Research*, *97*(B13), 19,683–19,715.
- Whitmarsh, R. B. (1971). Seismic anisotropy of the uppermost mantle absent beneath the east flank of the Reykjanes Ridge. *Bulletin of the Seismological Society of America*, *61*, 1351–1368.
- Wilkinson, C. M., Ganerød, M., Hendriks, B. W. H., & Eide, E. A. (2016). Compilation and appraisal of geochronological data from the North Atlantic Igneous Province (NAIP). In G. Peron-Pinvidic et al. (Eds.), *The NE Atlantic region: A reappraisal of crustal structure, tectonostratigraphy and magmatic evolution* (Vol. 447, pp. 69–103). London: Geological Society London Special Publication.
- Wright, J. D., & Miller, K. G. (1996). Greenland-Scotland Ridge control of North Atlantic Deep Water. *Paleoceanography*, *11*, 157–170.
- Wyllie, M., Gregory, A., & Gardner, L. (1956). Elastic wave velocities in heterogeneous and porous media. *Geophysics*, *21*, 41–70.